



HAL
open science

The preferential orientation of magnetic switchbacks and its implications for solar magnetic flux transport

Naïs Fargette, Benoit Lavraud, Alexis P. Rouillard, Victor Réville, Stuart D. Bale, Justin Kasper

► To cite this version:

Naïs Fargette, Benoit Lavraud, Alexis P. Rouillard, Victor Réville, Stuart D. Bale, et al.. The preferential orientation of magnetic switchbacks and its implications for solar magnetic flux transport. *Astronomy and Astrophysics - A&A*, 2022, 663, 10.1051/0004-6361/202243537 . insu-03867481

HAL Id: insu-03867481

<https://insu.hal.science/insu-03867481>

Submitted on 23 Nov 2022

HAL is a multi-disciplinary open access archive for the deposit and dissemination of scientific research documents, whether they are published or not. The documents may come from teaching and research institutions in France or abroad, or from public or private research centers.

L'archive ouverte pluridisciplinaire **HAL**, est destinée au dépôt et à la diffusion de documents scientifiques de niveau recherche, publiés ou non, émanant des établissements d'enseignement et de recherche français ou étrangers, des laboratoires publics ou privés.



Distributed under a Creative Commons Attribution 4.0 International License

The preferential orientation of magnetic switchbacks and its implications for solar magnetic flux transport

Naïs Fargette¹, Benoit Lavraud^{1,2}, Alexis P. Rouillard¹, Victor Réville¹, Stuart D. Bale^{3,4}, and Justin Kasper⁵

¹ Institut de Recherche en Astrophysique et Planétologie, CNRS, UPS, CNES, Toulouse, France
e-mail: nais.fargette@irap.omp.eu

² Laboratoire d'astrophysique de Bordeaux, Univ. Bordeaux, CNRS, Pessac, France

³ Space Sciences Laboratory, University of California, Berkeley, CA, USA

⁴ Physics Department, University of California, Berkeley, CA, USA

⁵ Climate and Space Sciences and Engineering, University of Michigan, Ann Arbor, MI, USA

Received 14 March 2022 / Accepted 5 May 2022

ABSTRACT

Context. Magnetic switchbacks in the solar wind are large deflections of the magnetic field vector, which often reverse their radial component, and are associated with a velocity spike consistent with their Alfvénic nature. The Parker Solar Probe (PSP) mission revealed them to be a dominant feature of the near-Sun solar wind. Where and how they are formed remains unclear and subject to discussion.

Aims. We investigate the orientation of the magnetic field deflections in switchbacks to determine if they are characterized by a possible preferential orientation.

Methods. We compute the deflection angles, $\psi = [\phi, \theta]^T$, of the magnetic field relative to the theoretical Parker spiral direction for encounters 1 to 9 of the PSP mission. We first characterize the distribution of these deflection angles for quiet solar wind intervals and assess the precision of the Parker model as a function of distance from the Sun. We then assume that the solar wind is composed of two populations, the background quiet solar wind and the population of switchbacks, the latter of which is characterized by larger fluctuations. We model the total distribution of deflection angles we observe in the solar wind as a weighed sum of two distinct normal distributions, each corresponding to one of the populations. We fit the observed data with our model using a Monte Carlo Markov chain algorithm and retrieve the most probable mean vector and covariance matrix coefficients of the two Gaussian functions, as well as the population proportion. This method allows us to quantify the properties of both the quiet solar wind and the switchback populations without setting an arbitrary threshold on the magnetic field deflection angles.

Results. We first confirm that the Parker spiral is a valid model for quiet solar wind intervals at PSP distances. We observe that the accuracy of the spiral direction in the ecliptic is a function of radial distance, in a manner that is consistent with PSP being near the solar wind acceleration region. We then find that the fitted switchback population presents a systematic bias in its deflections, with a mean vector consistently shifted toward lower values of ϕ (-5.52° on average) and θ (-2.15° on average) compared to the quiet solar wind population. This results holds for all encounters but encounter 6, and regardless of the magnetic field main polarity. This implies a marked preferential orientation of switchbacks in the clockwise direction in the ecliptic plane, and we discuss this result and its implications in the context of the existing switchback formation theories. Finally, we report the observation of a 12-hour patch of switchbacks that systematically deflect in the same direction, such that the magnetic field vector tip within the patch deflects and returns to the Parker spiral within a given plane.

Key words. solar wind – Sun: magnetic fields – Sun: corona – Sun: photosphere – methods: data analysis – methods: statistical

1. Introduction

Magnetic switchbacks are structures that are ubiquitous in the near-Sun solar wind and are particularly striking in the Parker Solar Probe (PSP) mission data (Kasper et al. 2019; Bale et al. 2019; Horbury et al. 2020; Dudok de Wit et al. 2020). Their in situ signatures include a large deflection of the magnetic field, which often reverses its radial component – hence the name; this deflection is associated with a velocity spike, which is consistent with their Alfvénic nature (Matteini et al. 2014; Phan et al. 2020). In addition, the magnetic field magnitude and the pitch-angle distribution (PAD) of the suprathermal electron population remain fairly constant within switchbacks (Kasper et al. 2019). From these observations, they are interpreted as large local magnetic folds with faster plasma superposed on a quieter solar wind (Bale et al. 2019). They have been observed more scarcely

in other mission data farther away from the Sun (Balogh et al. 1999; Gosling et al. 2011; Horbury et al. 2018) and are now known to be a significant feature of the solar wind below 0.3 AU.

Many physical processes have been proposed to explain the formation of these unexpected structures. One of the most investigated mechanisms is interchange reconnection (Nash & Sheeley 1988; Wang et al. 1989), where open field lines reconnect with closed ones in the low corona. The foot-point exchange of magnetic field lines provides a theoretical basis to explain how the magnetic field lines can sustain a quasi-rigid rotation in the corona while being anchored in a differentially rotating photosphere (Wang et al. 1996; Fisk 1996; Fisk et al. 1999). To keep up with the shear induced by the different rotation rates of the two domains, field lines reconnect at their base and allow coronal hole boundaries to remain unaffected by the photosphere differential rotation (Wang & Sheeley 2004;

Lionello et al. 2005, 2006). The newly reconnected magnetic configuration presents a folded magnetic field line, and Fisk & Kasper (2020) propose that this fold could propagate and become a magnetic switchback at PSP's orbit. However, how such folds could subsist in a low- β plasma is unclear, and variations around this mechanism have been proposed. Zank et al. (2020) argue that interchange reconnection may generate complex structures that propagate upward in the solar atmosphere and can reverse their radial field. Owens et al. (2018, 2020) and Schwadron & McComas (2021) propose that interchange reconnection may lead to a solar wind velocity gradient along open field lines. Subsequently, fast wind overcoming slower wind is able to reverse the magnetic field and create a fold beyond the Alfvén point. Drake et al. (2021) show through simulation that interchange reconnection can create magnetic flux ropes (FRs) that present switchback signatures (i.e., radial magnetic field component reversal), are very stable, and may subsist more easily through propagation in the solar corona and solar wind. Sterling & Moore (2020) investigate coronal jets as a source of switchbacks, arguing that reconnected, erupting mini-filament FRs could generate an Alfvénic fluctuation that steepens during propagation and becomes a switchback. All of these works assume that switchbacks are created in the low corona through magnetic reconnection. An alternative possibility is that switchbacks could be generated in situ through processes inherent to solar wind propagation. Ruffolo et al. (2020) argue that above the Alfvén point, shear-driven dynamics becomes dominant and accounts for the switchbacks observed by PSP, while Squire et al. (2020), Shoda et al. (2021), and Mallet et al. (2021) link switchbacks to solar wind turbulence. They use compressible magnetohydrodynamics simulations and show that expanding Alfvénic fluctuations eventually reverse the magnetic field radial component during propagation. These expanding fluctuations produce magnetic switchback signatures that are born purely out of turbulence in the solar wind.

The most recent data from PSP provided additional clues regarding the nature of switchbacks. An isotropization of the ion distribution function inside switchbacks was observed (Woodham et al. 2021), showing that plasma properties are different inside switchbacks. They also tend to aggregate in patches (Horbury et al. 2020; Dudok de Wit et al. 2020), and these patches are found to match the spatial scale of supergranulation (Fargette et al. 2021; Bale et al. 2021). In addition, switchback patches show an increase in alpha particle abundance compared to the background solar wind (Bale et al. 2021). All of these recent results indicate that switchback patches, and possibly switchbacks themselves, are distinct from the background solar wind, with different plasma properties, thereby pointing to a formation mechanism in the low corona.

In this work we investigate, over several PSP orbits, if the magnetic field deflections display a preferential orientation. Horbury et al. (2020) performed this type of analysis on a four-day period around the first perihelion of PSP. They report a tendency of long-duration switchbacks to deflect in the +T direction of the radial-tangential-normal (RTN) frame. They also highlight that nearby switchbacks tend to orient themselves in the same direction. A clockwise preference was also observed in switchbacks identified in Helios data by Macneil et al. (2020), and the same tendency was identified very recently by Meng et al. (2022) in encounters 1 and 2 in PSP data.

In Sect. 2 we present the data analyzed in this work, and detail the methodology and frame we use when defining the switchback phenomenon. In Sect. 3 we characterize the quieter background solar wind and quantify its dispersion around the

Parker spiral model. In Sect. 4 we model the solar wind as a superposition of a quiet background solar wind and a switchback population. We find that the latter displays a preferential deflection orientation. In Sect. 5 we present a particularly striking example of a patch of switchbacks that deflect systematically in the same direction and within the ecliptic plane for 12 h. In Sect. 6 we discuss our results in the context of the different existing formation theories and discuss implications on solar open flux transport. The conclusions of this study are then given in Sect. 7.

2. Data and methods

2.1. Data

The PSP mission was launched in August 2018 and is, at the time of writing, completing its 12th orbit around the Sun. During the past three years, the spacecraft scanned the solar wind gradually and increasingly deeper into the solar corona, as Venus gravity assists brought the perihelion of its highly elliptic orbit closer to the Sun. It reached in turn $35.6 R_{\odot}$ (0.166 AU, E_1 to E_3), $27.8 R_{\odot}$ (0.130 AU, E_4 to E_5), $20.3 R_{\odot}$ (0.095 AU, E_6 to E_7), and $16.0 R_{\odot}$ (0.074 AU, E_8 to E_9), where E_x stands for encounter (or orbit) number x .

In this study we analyze magnetic field and particle data taken by the different in situ instruments. Magnetic field data are provided by the FIELDS instrument suite (Bale et al. 2016) and the particle data by the Solar Wind Electrons Alphas and Protons (SWEAP) instrument suite (Kasper et al. 2016). Data from SWEAP include plasma moments from the Solar Probe Cup (Case et al. 2020) and plasma moments and electron PADs from the Solar Probe Analyzers (Whittlesey et al. 2020; Livi et al. 2021). All data were resampled to a constant time step of 2 s, and we limited our study to heliocentric radial distances of less than $60 R_{\odot}$. Data are shown in the RTN frame of reference, where \mathbf{R} (radial) is the Sun to spacecraft unit vector, \mathbf{T} (tangential) is the cross product between the Sun's spin axis and \mathbf{R} , and \mathbf{N} (normal) completes the direct orthogonal frame.

2.2. Switchback definition

In this work we aim to study statistically the orientation of switchbacks, as described in the introduction (Sect. 1). However, this poses a difficulty from the start. Indeed, switchbacks are usually identified as a deflection from a background magnetic field, and it is obvious that the choice of this background field directly affects the results one would obtain regarding their orientation. In the literature, various background definitions have been used to identify switchbacks in statistical studies, for instance: the radial direction (Woolley et al. 2020; Wu et al. 2021; Bourouaine et al. 2020; Mozer et al. 2020), a 6h median field (Dudok de Wit et al. 2020), a 6h mean field (Bandyopadhyay et al. 2021), a 1h mode field (Bale et al. 2019), and a modeled Parker spiral field (Horbury et al. 2020; Laker et al. 2021; Fargette et al. 2021). Various threshold were used, from 30 to 90°, as well as additional selection criteria such as duration, field magnitude, Alfvénicity, and density, which are not discussed here. Visual selections of switchbacks were also performed, often based on radial magnetic field reversals and their duration (Larosa et al. 2021; Martinović et al. 2021; Akhavan-Tafti et al. 2021).

Two kinds of approaches are typically used. One seeks to determine the background magnetic field through post treatment of the data in an attempt to differentiate switchbacks from

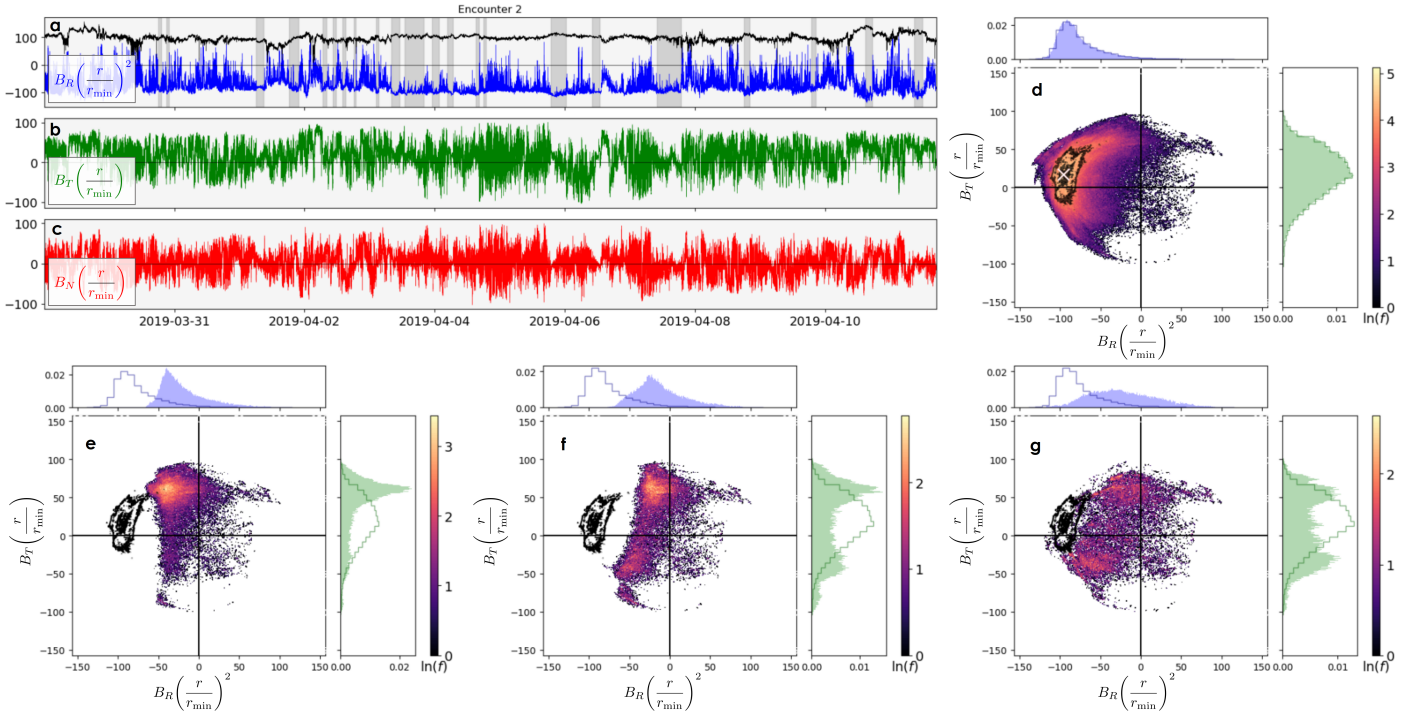


Fig. 1. Orientation of the magnetic field for PSP's second encounter. In panels *a*, *b*, and *c* we display the magnetic field components normalized by the radial distance $B_R(r/r_{\min})^2$, $B_T(r/r_{\min})$, and $B_N(r/r_{\min})$ (homogeneous to nT), with r the Sun-to-spacecraft distance and $r_{\min} = 35.6 R_{\odot}$ the radial distance at perihelion. The normalized magnetic field amplitude, $B(r/r_{\min})^2$, is displayed as well in black in panel *a*. The gray shaded intervals are manually selected quiet solar wind intervals (cf. Sect. 3). In panel *d* we plot the 2D distribution of $B_R(r/r_{\min})^2$ and $B_T(r/r_{\min})$, with the marginal distributions on the sides. Black contours surround the core of the distribution, and the color scale represents the number of samples. The average Parker spiral field over the encounter is marked as a white cross. In the bottom panels, we display the points located more than 60° away from the radial direction (*e*), the Parker spiral (*f*), and a 6-hour-mode vector (*g*), with the black contours a reminder of the core of the total distribution.

background solar wind, using different statistical parameters of the magnetic field distribution such as mean, median, or mode values. The other consists in modeling the expected background field independently using either a radial field assumption or the Parker spiral model. Both methods have their caveats. If the solar wind dynamics is dominated by switchbacks over long periods, as is often the case, then it is reflected in the mean, median, and mode value of the distributions considered, with associated biases. The appropriateness of the modeling approach, on the other hand, depends on the reliability of the model used and its potential limitations.

The backgrounds obtained through the use of these various methods can be drastically different and lead to different, and sometimes contradictory, results. In a study that focuses on the existence of a preferential orientation within switchback, it is essential to have in mind that this first assumption regarding background modeling may impact the results significantly. In Fig. 1 we illustrate this fact by comparing the different conclusions one might draw based on such selection processes. We display the magnetic field components measured by PSP in panels *a*, *b*, and *c* during E_2 , from 2019 March 29 at 00h to 2019 April 11 at 17h, when the spacecraft was below $60 R_{\odot}$. The B_R component is normalized by $(r/r_{\min})^2$, while B_T and B_N are normalized by (r/r_{\min}) , with r the Sun-to-spacecraft distance and $r_{\min} = 35.6 R_{\odot}$ the radial distance at perihelion. Here, PSP is connected to the negative polarity solar hemisphere throughout the 13 days of data. In the top-right panel *d*, we plot the 2D distribution of $B_R(r/r_{\min})^2$ and $B_T(r/r_{\min})$, with linearly spaced isocontours (black curves) underlining the core of the distribution. The color scale represents the number of samples, and we

also add the normalized projected distributions on the side. In the bottom panels *e* to *g*, we display the points that are located more than 60° away from the radial direction (*e*), the Parker spiral (*f*), and a 6-hour-mode vector (*g*), with the black contours a reminder of the core of the total distribution.

The core of the total distribution (black contours) has a nonzero B_T component. This positive B_T component is consistent with the Parker spiral. Indeed, when we take the average of the Parker spiral angle throughout the encounter (by taking the mean of Eq. (1) over E_2 ; see Sect. 2.3), we obtain an angle of $167 \pm 3^\circ$ from the radial direction. This corresponds to $B_T(r/r_{\min}) = 17 \pm 3$ nT and $B_R(r/r_{\min})^2 = -96 \pm 13$ nT, and we mark these values in panel *d* for illustrative purposes. In the following panels *e* to *g* it is clear that the distributions obtained through the three methods differ significantly. With the radial method, the B_T component of a modeled Parker spiral is neglected, and, as a direct consequence, the deviation one detects is strongly biased toward a positive B_T . By contrast, the distribution 60° away from the Parker spiral includes more points with a negative B_T while keeping a preference toward a positive B_T . Finally, when we set the switchback definition to 60° away from a sliding mode, the tangential distribution of the magnetic field is even more isotropic. From these plots, it is clear that if we want to investigate a possible systematic orientation, we cannot define switchbacks based solely on the radial direction because the tangential component of the Parker spiral is significant.

Defining switchbacks as a perturbation relative to the Parker spiral appears to be the most physically motivated approach for our purpose. In Fig. 1d we see that the spiral accurately models the core of the magnetic field orientation distribution. To study

deviations from a median or mode field may also be useful in some contexts, but this calls for a different interpretation of the results, as one would be studying rapid fluctuations as opposed to the slower fluctuations of the field. In this work we chose the Parker spiral as the modeled background field and checked for its accuracy before analyzing the switchback perturbation.

2.3. Coordinate system

The Parker spiral angle is the trigonometric angle between the radial direction and the spiral direction in the radial-tangential (RT) plane, given by (Parker 1958)

$$\alpha_p(t) = \arctan 2 \left(\frac{-\omega(r(t) - r_0)}{V_r(t)} \right), \quad (1)$$

where $\omega = 2.9 \times 10^{-6} \text{ s}^{-1}$ is the Sun's rotational frequency taken at the equator, $r(t)$ is the distance of the spacecraft to the center of the Sun, $r_0 = 10 R_\odot$ (Bruno & Bavassano 1997) is the source distance of the Parker spiral, and $V_r(t)$ is the measured radial speed of the solar wind. For our purpose, we used the velocity processed with a low pass filter characterized by a cutting wavelength at 2h. This allows for the removal of spurious data, as well as short timescale variations and transient structures that are not relevant to the Parker spiral angle. We thus obtained a Parker spiral angle that varies over time with a timestep of 2 s, which is similar to the timestep of other quantities.

To compare the magnetic field orientation to the expected local Parker spiral calculated with r and V_r , we transformed each data point into its local Parker frame, $\mathbf{x}, \mathbf{y}, \mathbf{z}$, where \mathbf{x} points in the direction of the local spiral, $\mathbf{z} = \mathbf{N}$ remains unchanged from the RTN frame, and \mathbf{y} completes the direct orthogonal frame. An important point is that this frame rotates as a function of the polarity of the solar magnetic field, and a magnetic field matching the local spiral perfectly is then written as $\mathbf{B} = B_x \mathbf{x}$, with B_x positive. Finally, when studying orientation, it is convenient to use a spherical coordinate system ($\|\mathbf{B}\|, \phi, \theta$), where ϕ and θ are the azimuthal and elevation angle in this xyz Parker frame spanning, respectively, $[-180, 180]^\circ$ and $[-90, 90]^\circ$. We hereafter write the vector containing the orientation angles of the magnetic field as $\boldsymbol{\psi} = [\phi, \theta]^\top$.

3. Quiet solar wind orientation

The first step of our study was to quantify the accuracy of the Parker model that we wanted to use for the background field. To do so, we manually selected periods of quiet solar wind in the time series as periods that were not dominated by large-scale fluctuations. We chose periods that lasted at least one hour with no or very few deviations greater than 60° from the expected spiral direction. This selection was performed visually, which may have led to a selection bias despite our best efforts. We hence give the timetable of the selected intervals in Appendix A, which are also illustrated Fig. 1 for E_2 . In Fig. 2 we display the distribution of the orientation angles ϕ and θ inside these quiet solar wind intervals, with the colors differentiating the different encounters.

The magnetic field orientation in these quiet solar wind intervals matches the Parker spiral direction given by $\boldsymbol{\psi} = [0^\circ, 0^\circ]^\top$ reasonably well¹. The statistical parameters of the

¹ To give the reader a range of comparison, this $\boldsymbol{\psi} = [0^\circ, 0^\circ]^\top$ direction corresponds to angles relative to the radial direction between 5.6° and 29.6° depending on r and V_r .

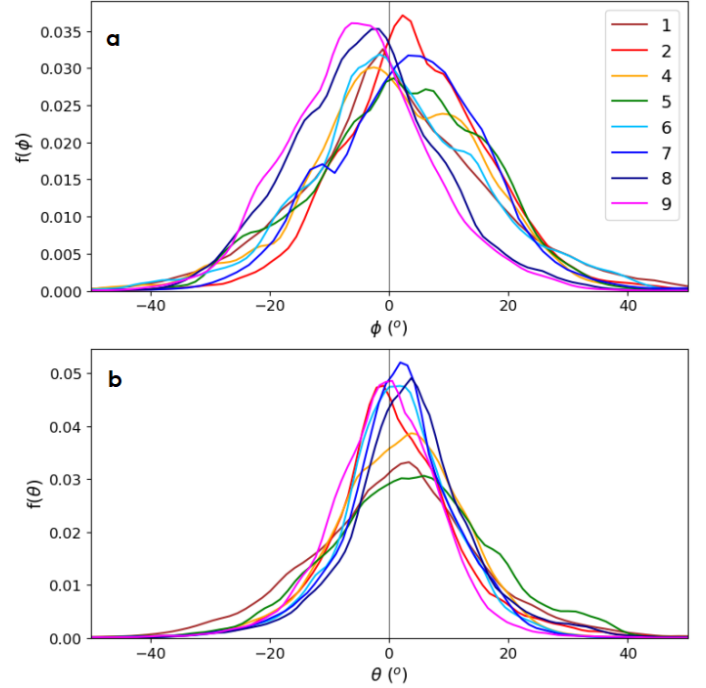


Fig. 2. Distributions of orientation angles ϕ (panel a) and θ (panel b) for quiet solar wind intervals over encounters 1 to 9.

Table 1. Median vectors and associated dispersion of the quiet solar wind distributions displayed in Fig. 2.

Enc	$\boldsymbol{\psi}$ Median ($^\circ$)	$\boldsymbol{\psi}$ Dispersion ($^\circ$)
1	[0.4, 1.2]	[16.6, 14.6]
2	[4.0, 0.5]	[12.7, 11.2]
4	[0.8, 2.1]	[14.3, 10.8]
5	[2.4, 3.7]	[14.5, 13.9]
6	[1.1, 1.7]	[14.8, 9.7]
7	[3.7, 1.8]	[13.4, 10.2]
8	[-3.9, 3.3]	[12.5, 10.7]
9	[-5.3, -0.4]	[12.0, 9.7]

distributions are given in Table 1, with on average a median vector of $[0.4^\circ, 1.8^\circ]^\top$ and associated standard deviations of $[13.9^\circ, 11.3^\circ]^\top$. Interestingly, we note a tendency for E_8 and E_9 to have a median value and peak biased toward negative ϕ . We investigated if this could be due to PSP approaching closer to the Sun for the latest encounters. In Fig. 3 we plot for each quiet solar wind interval the median orientation of the angles ϕ (panel 3a) and θ (panel 3b) as a function of the spacecraft distance r (gray dots), and we add the associated standard deviation (gray bars). We find a Spearman correlation coefficient (which measures the degree of monotonicity between two variables) of 0.28 for (ϕ, r) with an associated p -value of 3×10^{-4} , and of 0.05 for (θ, r) with an associated p -value of 0.5. Even though the correlation coefficient of ϕ with r is low, the small p -value indicates that the probability of observing such a data set with randomly distributed variables is 3×10^{-4} (and as such, unlikely). This shows that, although weak, the correlation between ϕ and r seems significant, while that between θ and r does not. We also fit a linear model to the data and find that $\phi = 0.235^{+0.081}_{-0.128} r - 6.0^{+3.3}_{-4.4}$ and $\theta = 0.049^{+0.072}_{-0.122} r + 0.4^{+3.8}_{-3.3}$, once again confirming that ϕ slightly increases with distance, r . The

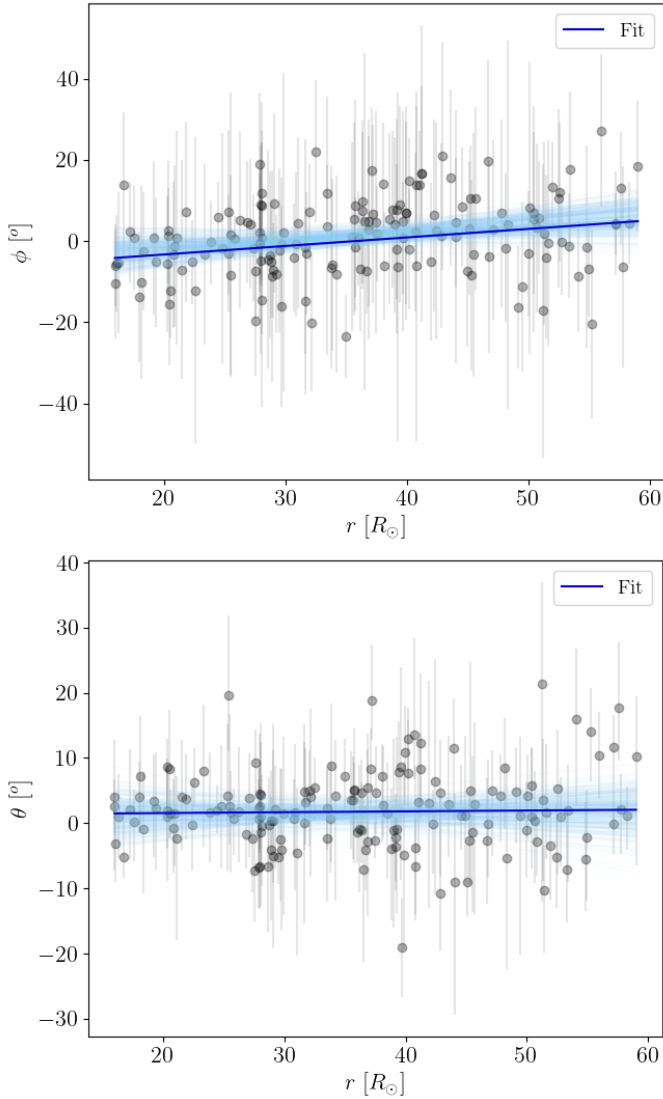


Fig. 3. Orientation angles of the quiet solar wind intervals given in Table 1 as a function of radial distance to the Sun. The median value of each interval is plotted (gray dots) with the dispersion inside the interval (error bar).

fits are shown in Fig. 3, with the uncertainty of the fit indicated. This does not necessarily mean that the relation between the two variables is linear, as indeed the increase is mainly visible below $30 R_{\odot}$ and in data from E_8 and E_9 . This result should be confirmed by measurements from further encounters; nonetheless, we discuss its implications in Sect. 6.1.

4. Global orientation

4.1. Modeling switchbacks

We next considered the complete 2D distribution of magnetic field orientation angles for E_2 , $f(\boldsymbol{\psi})$, which spans 13 days of data with a 2-second timestep. It is displayed in Fig. 4a together with the marginal (i.e., projected) distributions of ϕ (4b) and θ (4c). The distribution is characterized by a median vector of $\boldsymbol{\psi} = [-2.9^{\circ}, 1.4^{\circ}]^T$ (black lines in 4b and c) with an associated standard deviation of $[34.7^{\circ}, 22.6^{\circ}]^T$, hence wider than the quiet solar wind distribution and consistent with the presence of a population of larger fluctuations. We can see that the peak of the

distribution remains around $[0^{\circ}, 0^{\circ}]^T$, as it was for the quiet solar wind.

A usual method chosen to study switchbacks is to segregate the two populations – background wind and switchbacks – based on a chosen threshold angle. Given the quiet solar wind distribution displayed in Fig. 2, we find that this threshold should be taken at a minimum of around 40° (three standard deviations away) in the ϕ direction. This threshold is usually taken on the angle between \mathbf{B} and \mathbf{x} (with \mathbf{x} the unit vector of the Parker spiral; see Sect. 2.3), which is linked to ϕ and θ through $\mathbf{b} \cdot \mathbf{x} = \cos \theta \cos \phi$, with \mathbf{b} the unit vector of \mathbf{B} . In panel 4a we draw the limit corresponding to a 60° threshold angle, characterized by $\cos \theta = (2 \cos \phi)^{-1}$, and we overlay the distribution of the points outside this limit in panels b and c. These points are characterized by a median vector of $[-54.7^{\circ}, -6.2^{\circ}]^T$ (blue lines in 4b and c) and with associated standard deviations $[79.6^{\circ}, 43.4^{\circ}]^T$. We notice that large-scale fluctuations occur in all directions around the Parker spiral angle and that their distribution is biased toward negative values of ϕ and θ , which correspond to the +T and -N directions in a magnetic field of negative polarity. By construction, in this threshold approach the switchback distribution (in blue) is a truncated distribution. In the rest of the analysis we adopted a more continuous probabilistic approach, considering the superposition of two solar wind populations with distinct normal distributions in deflection angles. Importantly, we underline here that both methods – segregation or mixing and fitting of the two populations – find consistent results in terms of switchback preferential direction.

For the second approach, we assumed that the wind was composed of two populations with distinct distribution properties, respectively representing the background, quiet solar wind and the population of switchbacks characterized by larger fluctuations. In accordance with the results of Sect. 3, we assumed that the quiet solar wind magnetic field deflections followed a 2D normal distribution, $\mathcal{N}(\boldsymbol{\mu}_0, \boldsymbol{\Sigma}_0)$, that should remain close to the Parker spiral, together with a superposed second population of larger deflections, $\mathcal{N}(\boldsymbol{\mu}, \boldsymbol{\Sigma})$, that represents the switchbacks, where $\boldsymbol{\mu}$ and $\boldsymbol{\Sigma}$ are respectively the mean vector and the covariance matrix of the considered distributions. The total distribution we observe in Fig. 4 can then be modeled by the sum of the two normal distributions, weighted with a given proportion γ . This model is written as

$$f_m(\boldsymbol{\psi}, \mathbf{P}) = (1 - \gamma) \mathcal{G}(\boldsymbol{\psi}, \boldsymbol{\mu}_0, \boldsymbol{\Sigma}_0) + \gamma \mathcal{G}(\boldsymbol{\psi}, \boldsymbol{\mu}, \boldsymbol{\Sigma}), \quad (2)$$

where f_m is the modeled distribution, $\mathcal{G}(\boldsymbol{\psi}, \boldsymbol{\mu}_0, \boldsymbol{\Sigma}_0)$ and $\mathcal{G}(\boldsymbol{\psi}, \boldsymbol{\mu}, \boldsymbol{\Sigma})$ are 2D Gaussian functions of respective mean vectors $\boldsymbol{\mu}_0 = [\mu_{0\phi}, \mu_{0\theta}]^T$, $\boldsymbol{\mu} = [\mu_{\phi}, \mu_{\theta}]^T$ and covariance matrices $\boldsymbol{\Sigma}_0 = \text{diag}(\sigma_{0\phi}, \sigma_{0\theta})$, $\boldsymbol{\Sigma} = \text{diag}(\sigma_{\phi}, \sigma_{\theta})$, and \mathbf{P} is the parameter vector to the fit and contains nine parameters:

$$\mathbf{P} = [\mu_{0\phi} \quad \mu_{0\theta} \quad \sigma_{0\phi} \quad \sigma_{0\theta} \quad \mu_{\phi} \quad \mu_{\theta} \quad \sigma_{\phi} \quad \sigma_{\theta} \quad \gamma]^T. \quad (3)$$

We assumed that our data (i.e., the distribution f) followed our model f_m with a white noise model, and we take the associated dispersion, σ_{ϵ} , to be 10% of the maximum of f . From hereon, for a given set of parameter \mathbf{P} , the likelihood of the data follows a 2D normal distribution and can be written as

$$p(f | \boldsymbol{\psi}, \mathbf{P}) = \mathcal{G}(f, f_m(\boldsymbol{\psi}, \mathbf{P}), \sigma_{\epsilon} \mathbb{1}), \quad (4)$$

where $p(X)$ designates the probability of X and $\mathbb{1}$ is the identity matrix. We used uniform priors $p(\mathbf{P})$ on all of the parameters, with the constraints $\mu_{0\phi}, \mu_{0\theta} \in [-10^{\circ}, 10^{\circ}]$, $\sigma_{0\phi}, \sigma_{0\theta} \in [0.1^{\circ}, 30^{\circ}]$. These constraints are based on the results from

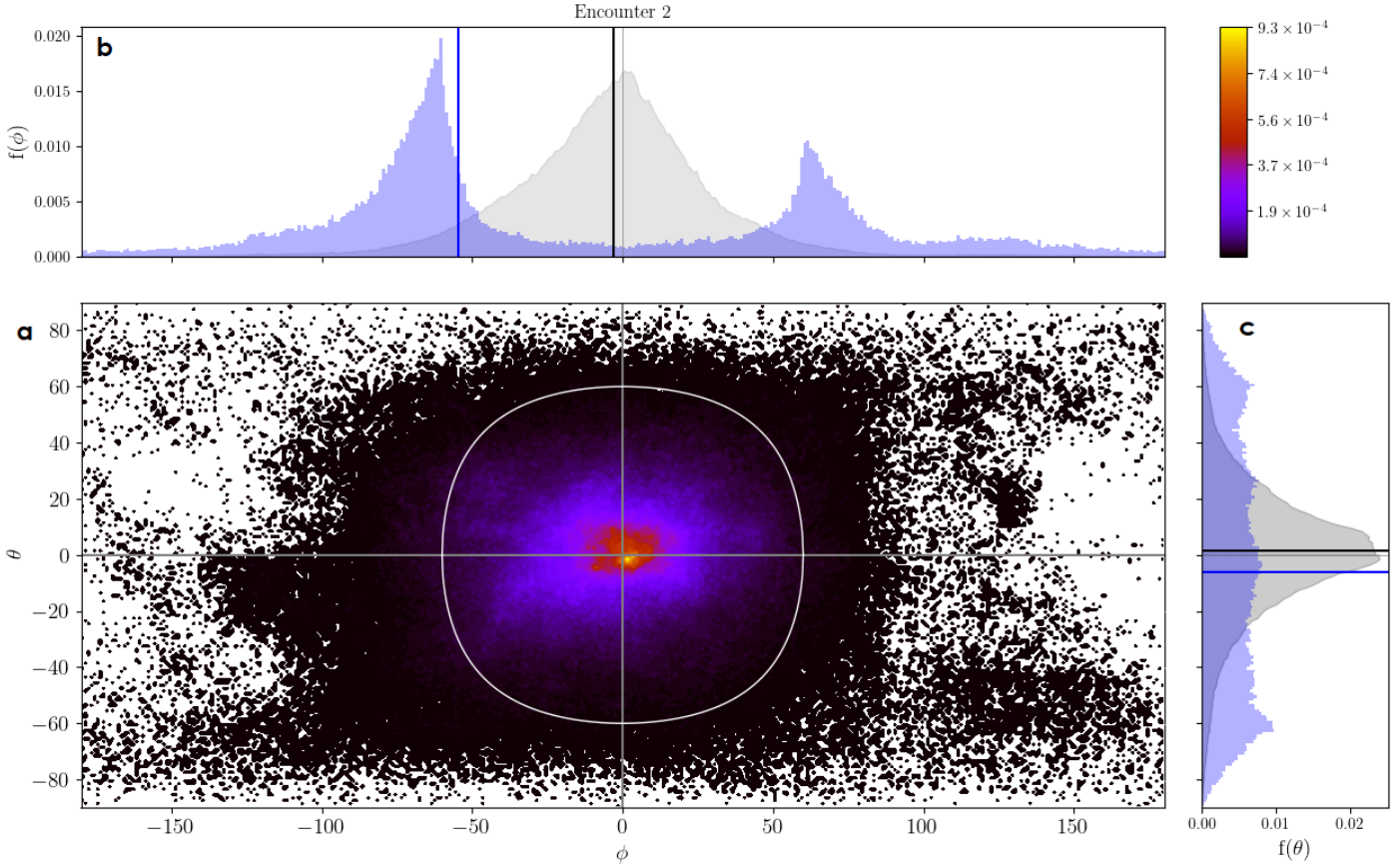


Fig. 4. 2D normalized distribution of magnetic field orientation angles for E_2 (panel *a*) together with the marginal distributions of ϕ and θ in light gray in panels *b* and *c*. Black lines indicate the median values of the marginal distributions. The white line in panel *a* corresponds to a 60° threshold angle (see the text for more details), and in panels *b* and *c* we overlay in light blue the distribution of the points outside this line. The blue lines indicate the median values of these truncated blue distributions.

Sect. 2, where we find a mean close to zero and a dispersion of around 15° .

We can now find the most probable parameters to fit our distribution and hence seek to maximize the log-posterior probability of the model through the Bayes equation:

$$\ln p(\mathbf{P} | \boldsymbol{\psi}, f) = \ln p(\mathbf{P}) + \ln p(f | \boldsymbol{\psi}, \mathbf{P}) + C, \quad (5)$$

where C is a constant.

We sampled the parameter space using the *emcee* python library (Foreman-Mackey et al. 2019), which is based on a Monte Carlo Markov chain algorithm, using 32 walkers and 2000 iterations. In Appendix C we display the convergence of the 32 walkers over the 2000 iterations (Fig. C.1) and show the probability distribution function of the walker positions in 9D space, discarding the first 1000 iterations (Fig. C.2). This yields the most probable parameter vector \mathbf{P} , which is summarized in Table 2.

In Fig. 5 we present the 2D distribution of the magnetic deflection angles in the same manner as in Fig. 4, together with the fitting result. In panel 5a we show the fitted function corresponding to the parameters in Table 2, together with the marginal distribution in panels b and c. We also plot in panels b and c the projected quiet solar wind distribution $(1 - \gamma) * \mathcal{G}(\boldsymbol{\psi}, \boldsymbol{\mu}_0, \boldsymbol{\Sigma}_0)$ and the switchback distribution $\gamma * \mathcal{G}(\boldsymbol{\psi}, \boldsymbol{\mu}, \boldsymbol{\Sigma})$. To give a sense of the fit precision, we also plot a hundred similar functions with parameters drawn randomly from the parameter probability distribution displayed in Fig. C.2. Finally, we display the quiet solar

Table 2. Most probable (maximum a posteriori) parameter vector \mathbf{P} , obtained after fitting the double Gaussian model described in the text to the data from E_2 .

$\mu_{0\phi}$	$\mu_{0\theta}$	$\sigma_{0\phi}$	$\sigma_{0\theta}$
$1.61^{+0.23}_{-0.18}$	$1.81^{+0.14}_{-0.12}$	$11.32^{+0.32}_{-0.28}$	$7.44^{+0.15}_{-0.19}$
μ_ϕ	μ_θ	σ_ϕ	σ_θ
$-5.68^{+0.42}_{-0.48}$	$1.71^{+0.29}_{-0.25}$	$31.75^{+0.43}_{-0.44}$	$22.13^{+0.29}_{-0.42}$
γ			
$0.7975^{+0.0095}_{-0.0094}$			

Notes. The first line presents the parameters associated with the background quiet solar wind model, the second line those associated with the switchback population, and the third line the proportion of the switchback population.

wind distribution found for E_2 as displayed in Fig. 2 but multiplied by $(1 - \gamma)$ so that the scales are comparable.

What is striking is first that the fitted function (in black in panels b and c) follows the 2D data distribution quite well, and second that the fitting algorithm finds a Parker spiral distribution (in red in panels b and c) with characteristics very similar to the one found in Sect. 2 in an independent manner (see Table 1 line 2 and Table 2 line 1). We can see that, as expected, the switchback population presents a larger dispersion in both dimensions. Its

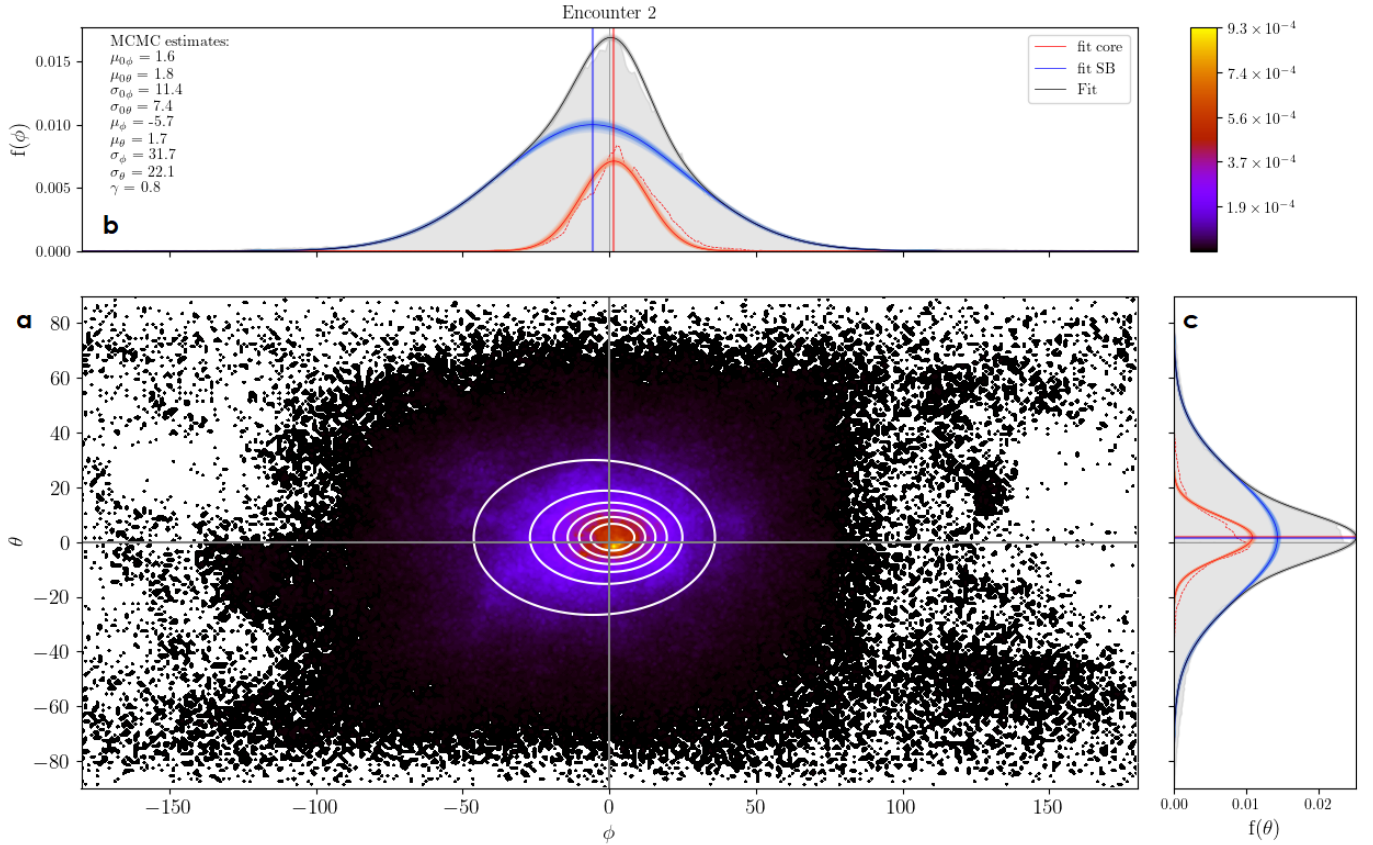


Fig. 5. 2D distribution of magnetic field orientation angles for E_2 (panel *a*) together with the marginal distributions of ϕ and θ in light gray in panels *b* and *c*. The white contours in panel *a* represent the fitted function, and its marginal distributions are in black in panels *b* and *c*. We also plot in panels *b* and *c* the marginal distributions corresponding to quiet solar wind (red) and switchback (blue) populations, with lines indicating their mean. The curves in lighter red, blue, and black give a sense of the fit precision. Finally, in dashed red we display the quiet solar wind distribution found for E_2 2 as displayed in Fig. 2 but multiplied by $(1 - \gamma)$ so that the scales are comparable. See the text for more detail.

mean vector, however, is different from that of the quiet solar wind population. It presents a negative value in the ϕ dimension, $\mu_{\phi} = -5.68^{+0.42}_{-0.48}$. This negative μ_{ϕ} is consistent with the result found with the previous method (Fig. 4) when we considered the median of points with a large deviation from the Parker spiral. In the θ dimension, however, we find no difference between the means of the core and the switchback population, while in the previous method we had found a slight tendency toward negative θ . This discrepancy can be explained by the fact that the tail of the marginal distribution in negative θ is not reproduced by the fit well (panel 5c). Finally, we find that the proportion of the switchback population in the solar wind is close to 80%. This high proportion is due to the method we are using and can be interpreted as the proportion of the observed solar wind that is dominated by magnetic switchbacks.

To summarize, in our method we assumed that the solar wind magnetic field fluctuations were composed of two populations, each with orientation angles that followed a 2D normal distribution. The first is assumed to follow the Parker spiral with a rather small dispersion, and the second is the switchback population with a wider dispersion. After fitting this model to our data, we find that the background population we retrieve is consistent with the quiet solar wind distribution described in Sect. 3. We also find that the switchback population is biased, with an offset in the $-\phi$ direction. These results are confirmed with the more simple analysis we performed in Fig. 4, where we analyze the median values of points more than 60° away from the spiral and also find a preferential $-\phi$ orientation.

4.2. A systematic bias in the deflections

We next applied the same method to the remaining encounters. For each, we considered the available data below $60R_{\odot}$ and discarded intervals where the Parker spiral model is not relevant, that is, where we identified heliospheric current sheet (HCS) crossings, coronal mass ejections (CMEs) or FRs. This selection was done manually by analyzing the magnetic field, plasma moments, and the PAD of suprathermal electrons; it can be reviewed in Appendix B. In order to identify a potential influence of the magnetic field polarity, we also restrained our study to the main polarity of each encounter. This means that we considered only the data points when the spacecraft was sampling a negative polarity solar wind (south of the HCS) for encounters 1, 2, 4, 5, 6, and 9, and a positive polarity solar wind (north of the HCS) for encounters 7 and 8. We computed the orientation angles of the magnetic field in the local Parker frame and fit the obtained distribution for the most probable parameters in the same manner as in Table 2.

The results are summarized in Figs. 6 and 7 and available in full in Appendix C. In Fig. 6 we display all the fits we performed for the different encounters by looking at the marginal distributions. We plot $f(\phi)$ and $f(\theta)$, which correspond to the marginal distributions of the magnetic field orientation observed by PSP for each encounter. We show the fitted marginal distributions of the quiet solar wind (in red) and the switchbacks (in blue), with vertical colored lines indicating their mean value. We note that the plots shown for E_2 in Fig. 6 are the same as the ones

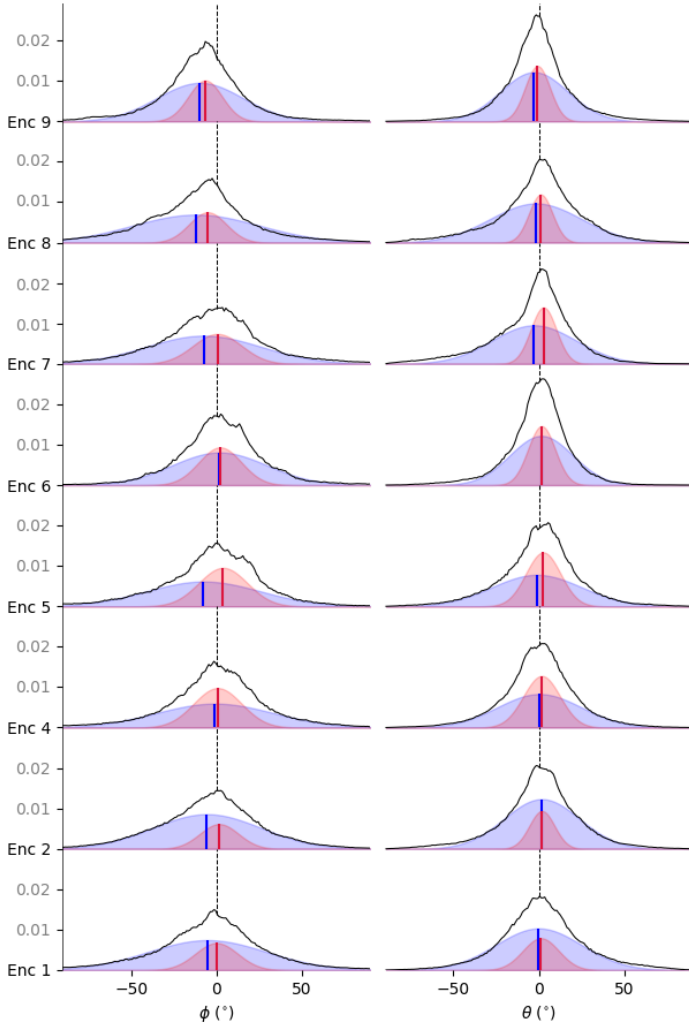


Fig. 6. Marginal distributions of observed magnetic field orientation angles $f(\phi)$ (a) and $f(\theta)$ (b) displayed in black for all encounters, with a shared y axis. The fitting results are also plotted: in light red the marginal distributions corresponding to quiet solar wind, and in light blue the marginal distribution corresponding to switchbacks. Vertical lines indicate their mean, and the dashed line in the background is the zero value.

detailed in Figs. 5b and c. This visualization shows that, to first order, the data are accurately reproduced by the model we use (i.e., the weighed superposition of two Gaussian functions). We also see that the switchback distribution (in blue) clearly shows a biased mean shifted toward smaller values of ϕ (and θ to a lesser degree) compared to the quiet solar wind, for all encounters independently apart from E_6 .

In Fig. 7 we display a scatter plot of the mean vector of each population for all encounters. We show the mean vectors found for the quiet solar wind population $\boldsymbol{\mu}_0 = [\mu_{0\phi}, \mu_{0\theta}]^T$ (corresponding to the red vertical lines in Fig. 6) and the mean vectors found for the switchback population $\boldsymbol{\mu} = [\mu_\phi, \mu_\theta]^T$ (vertical blue lines in Fig. 6). Each couple of points is linked by a line for visualization purposes. Finally, contours around the markers (filled for quiet solar wind, transparent for switchbacks) indicate the uncertainty (1σ) of the fit we performed. For E_8 and E_9 the quiet solar wind means have negative ϕ values, which is consistent with the values presented in Sect. 2. The shifts between the means of the quiet solar wind and switchback distributions are given for each encounter in Table 3, with $\Delta\mu_\phi = -5.52^\circ$ and $\Delta\mu_\theta = -2.15^\circ$ on

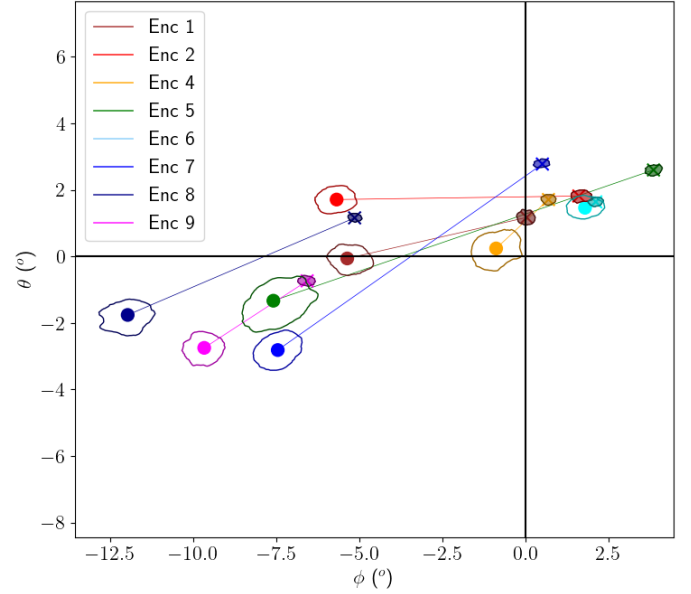


Fig. 7. Mean vectors of the quiet solar wind (cross) and switchback (dot) populations for each encounter. Both are linked by a line for visualization purposes. Contours around the markers (filled for quiet solar wind, transparent for switchbacks) indicate the uncertainty of the fit we performed.

Table 3. Shift between the quiet solar wind and switchback distribution means.

Enc	$\Delta\mu_\phi$ ($^\circ$)	$\Delta\mu_\theta$ ($^\circ$)
1	-5.41	-1.22
2	-7.25	-0.11
4	-1.60	-1.38
5	-11.47	-3.81
6	-0.37	-0.18
7	-8.06	-5.58
8	-6.86	-2.87
9	-3.12	-2.02
$\langle \cdot \rangle$	-5.52	-2.15

Notes. The last line is the average over all encounters.

average. For all encounters except E_6 , the switchback population is shifted significantly to lower values of ϕ , while for all encounters except E_2 and E_6 it is also somewhat shifted toward lower values of θ , although the trend is less significant. These results are further discussed in Sect. 6.2.

5. Case study of a unidirectional planar patch of switchbacks

In addition to the large-scale systematic bias found over the different encounters (Sect. 4), we want to highlight in this section that on smaller scales switchbacks can be deflected very consistently in the same direction. As such, we report on a patch of switchbacks that occur during E_2 from 2020 April 5 at T20:00 to 2020 April 6 at T12:00, for a total duration of 16 h, which is displayed in Fig. 8. In the top panel we display the radial and tangential component of the magnetic field, B_R and B_T , as well as the expected components of the Parker spiral magnetic field. The difference between model and data is indicated. In the

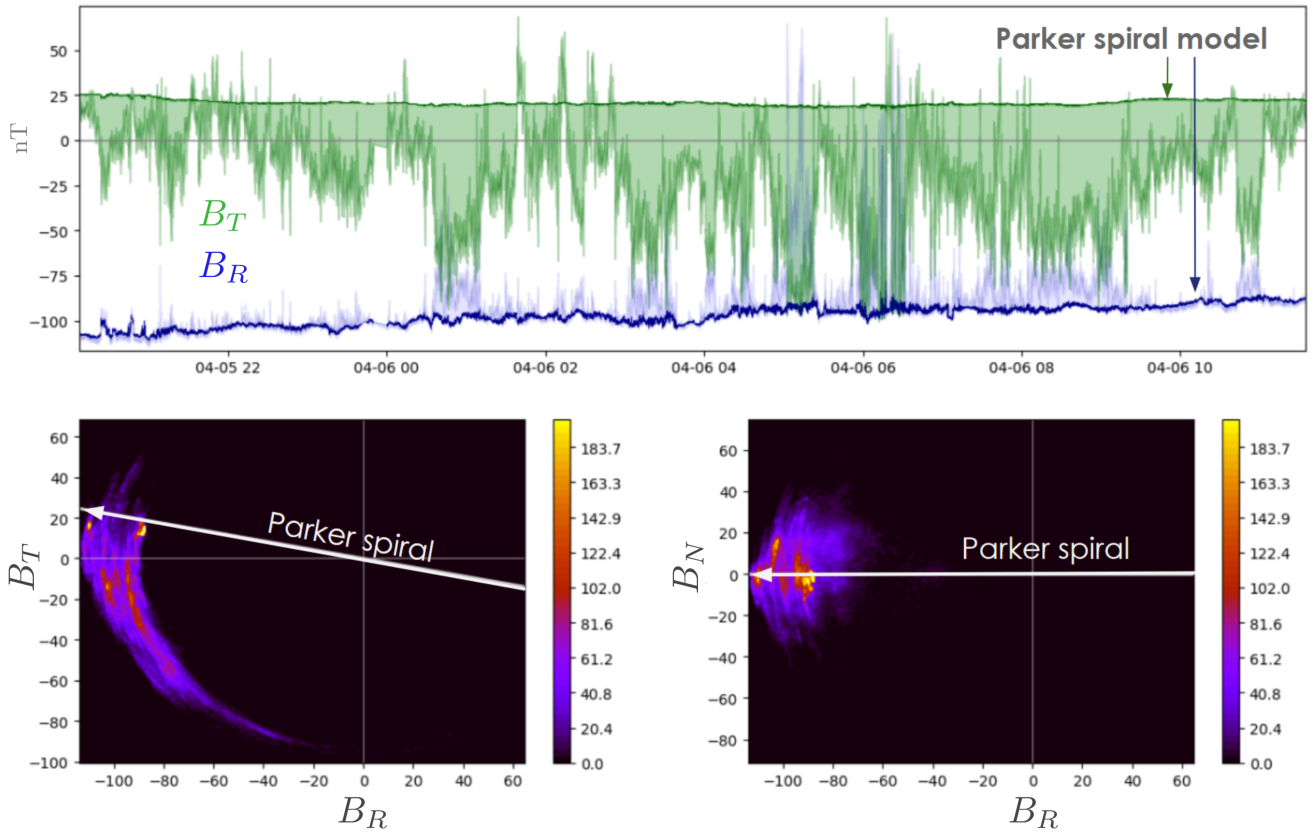


Fig. 8. Illustration of a one-sided patch of switchbacks. *Top panel:* radial and tangential component of the magnetic field, B_R and B_T , as well as the expected components of the Parker spiral magnetic field. The difference between model and data is lightly shaded. In the *bottom panels*, we plot the 2D distributions $f(B_R, B_T)$ and $f(B_R, B_N)$; the color scale indicates the number of points inside each bin.

bottom panels, we plot the 2D distribution $f(B_R, B_T)$ and $f(B_R, B_N)$. An arrow indicates the average expected direction of the Parker spiral. In these plots, it is clear that the magnetic field deviates in one direction during the entire patch, which is B_T negative in the ecliptic plane. This corresponds to the $+\phi$ direction with the notation adopted in this paper. The path taken to deflect and return to the Parker spiral remains unchanged within a given plane (here the ecliptic) rather than moving randomly in three dimensions.

This further confirms the results from Horbury et al. (2020), who find that the larger switchbacks within a patch tend to deflect in the same direction. Here we do not have a notion of switchback duration but show that deviations are contained within the ecliptic plane ($\theta < 30^\circ$, not shown) and are one-sided with regard to the Parker spiral ($+\phi$ direction). This event interestingly goes in the opposite direction compared to the systematic bias we find in Sect. 4. This is not unexpected, as the data displayed in Figs. 4 to 6 show that switchbacks may deflect in any direction despite the average having a tendency toward negative ϕ .

6. Discussion

6.1. Parker spiral

We show in Sect. 3 that as PSP's distance to the Sun decreases, the magnetic field data of quiet solar wind intervals seem to deviate from the Parker spiral model predictions. This is mainly visible in the data from E_8 and E_9 , when PSP was diving down to $16R_\odot$ at perihelion (while data above $30R_\odot$ show no obvi-

ous trend, which is consistent with the results in Badman et al. 2021). Geometrically, this means that we are overestimating the algebraic value of the Parker spiral angle, α_p , and that the spiral is wound less tightly than expected. The Parker spiral model computed in the present study is given by Eq. (1), with $\omega = 2.9 \times 10^{-6} \text{ s}^{-1}$, $r_0 = 10R_\odot$, and where $V_r(t)$ is the measured radial speed of the solar wind processed with a 2 h low pass filter. However, this model implicitly assumes a constant solar wind speed between the source surface of radius r_0 and the spacecraft, and this hypothesis is likely no longer valid so close to the Sun, especially in the slow solar wind that accelerates until 10–20 solar radii (see, e.g., Bruno & Bavassano 1997). With these values in mind, and seeing that the average value of solar wind speed during E_8 and E_9 is around 200 to 300 km s^{-1} , it is highly probable that at such heights, PSP is located within the acceleration region of the solar wind; recently, Kasper et al. (2021) reported that PSP even went down to the magnetically dominated corona during its latest orbits. This is consistent with our results, since the spiral we observe is straighter than the expected Parker spiral associated with the wind speed measured by PSP. Indeed, overestimating the algebraic value of α_p amounts to overestimating the value of the solar wind speed, V_r , from the source.

6.2. Switchback orientation

In Sect. 4 we show that for all encounters (with the exception of E_3), the switchback population presents a preferential deflection orientation toward lower values of the ϕ and θ angles. This result holds for all encounters (albeit being less clear in E_6) and is not impacted by the polarity of the magnetic field. We

highlight the implication of this result in a more visual manner in Fig. 9. In this sketch we represent in panel a a top view of the Sun (N is in the out-of-plane direction), two field lines with positive (red) and negative (blue) polarity, and the associated Parker frame at a given radius as previously defined in Sect. 2.3. It is easier to see in this visualization that for a positive field, negative ϕ values correspond to the $-T$ direction, while for a negative polarity field it corresponds to the $+T$ direction (except for very large deflections close to $-\pi$, where the T component would reverse in both cases); both of these situations correspond to a clockwise rotation. This is consistent with the results of Horbury et al. (2020), who stated that switchbacks present a preferential orientation in the $+T$ direction during E_1 , where PSP mainly samples the negative polarity hemisphere of the Sun. This clockwise preference was observed in Helios data by Macneil et al. (2020) and more recently identified by Meng et al. (2022) in E_1 and E_2 in PSP data, which further confirms our result. In Fig. 9 we draw a switchback illustration consistent with the negative ϕ preference for each polarity, and one can see that the geometry remains unchanged. In addition, switchbacks are both accelerated structures (sometimes called “velocity spikes” due to their associated increase in V_r ; Kasper et al. 2019) and Alfvénic properties. Hence, in the negative (respectively positive) magnetic sector, the magnetic field is correlated (anticorrelated) with the velocity vector. This leads to the field line configurations displayed in Fig. 9, which are associated with positive tangential flows. On the other hand, the less marked bias toward $-\theta$ values corresponds to the $-N$ direction regardless of the polarity. One can realize that, in this case, this indicates a symmetry of the switchback geometry in the two hemispheres. We illustrate this configuration in panel b, with a side view of the Sun (T is in the in-plane direction) and a switchback with negative B_N for each polarity. To summarize, we find that switchbacks – viewed as a population of large magnetic deflections with respect to the Parker spiral – occur in all directions, while their deflection distribution presents a systematic bias in the $-\phi$ direction and to a lesser extent in the $-\theta$ direction. We now discuss this result in light of the existing potential formation process for magnetic switchbacks presented in the introduction.

6.3. Possible interpretation

Interchange reconnection is a mechanism that allows the open magnetic field lines of the Sun to reconnect at their base with closed loops that emerge from the magnetic carpet. This phenomenon mitigates the shear induced by the differential rotation of the photosphere – where field line footpoints rotate at different speeds depending on latitude – and the quasi-rigid rotation of the corona at equatorial rates due to force balance with the large-scale coronal structure, including transients (Wang et al. 1996; Fisk 1996; Fisk et al. 1999; Wang & Sheeley 2004; Lionello et al. 2005, 2006). In the reference frame of a coronal hole that is corotating quasi-rigidly at the equatorial rotation rate, magnetic loops appear to drift in the direction opposite to that of solar rotation, from west to east. This relative drift can induce strong magnetic shears that force magnetic reconnection between magnetic loops and open field lines. Subsequently, this leads to a footpoint displacement due to magnetic reconnection favored in the direction of solar rotation. Of course, if the photosphere is somehow going faster than the corona (locally, near the equator, for instance), then the favored motion is reversed. In general, however, the process may be random and in all directions for the majority of the events because of localized pho-

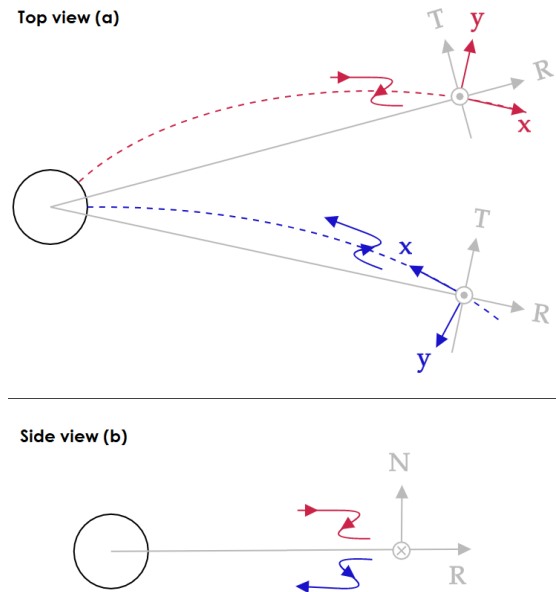


Fig. 9. Illustration of the favored geometry of switchbacks in negative (blue) and positive (red) polarity.

tospheric motions associated with the magnetic carpet and solar granulation. The phenomenology at stake is illustrated in Fig. 10. There, the sketch displays an element of open flux tubes from the photosphere expanding out into a faster corona, inducing a shear in the magnetic field lines as just described. The sketch is valid for all such flux bundles that escape from the otherwise mixed polarity patchwork of closed field lines of the magnetic carpet. At the bottom of the flux tube, magnetic reconnection can occur randomly and in all directions between the open field lines and closed loops that emerge from the magnetic carpet. As the photosphere lags behind the solar corona, a particular geometry could be favored as footpoint motion tends to mitigate the speed shear and jump in the direction of solar rotation. We suggest that this process could induce the bias in switchback orientation we present in this paper. This is consistent with Bale et al. (2021), who also interpret E_6 data in terms of a shear between the photosphere and corona.

Our results seem to be consistent with such reconnection occurring in regions where the photosphere is going, on average, slower than the solar corona, which would lead to the geometry highlighted in Figs. 9a and 10. This situation of a slower photosphere is particularly valid at mid to higher latitudes, typically over 30° in latitude, as studies of the coronal hole rotation rate indicate (e.g., Giordano & Mancuso 2008; Mancuso & Giordano 2011; Bagashvili et al. 2017; Mancuso et al. 2020). However, analysis of the spacecraft connectivity throughout E_1 indicates that the measured solar wind observed by PSP was emerging from an equatorial coronal hole (Bale et al. 2019; Badman et al. 2020; Réville et al. 2020), which would supposedly rotate close to the photospheric speed. We thus expect a lower $-\phi$ bias in this case. Nonetheless, we must consider the small but existing latitudinal extent of the coronal hole, as well as potential additional solar wind sources, in the interpretation of E_1 data. Future work on the connectivity of PSP during switchback observation is needed for the different encounters, to confirm or rule out a potential link between the $-\phi$ bias and the interchange reconnection induced by differential rotation.

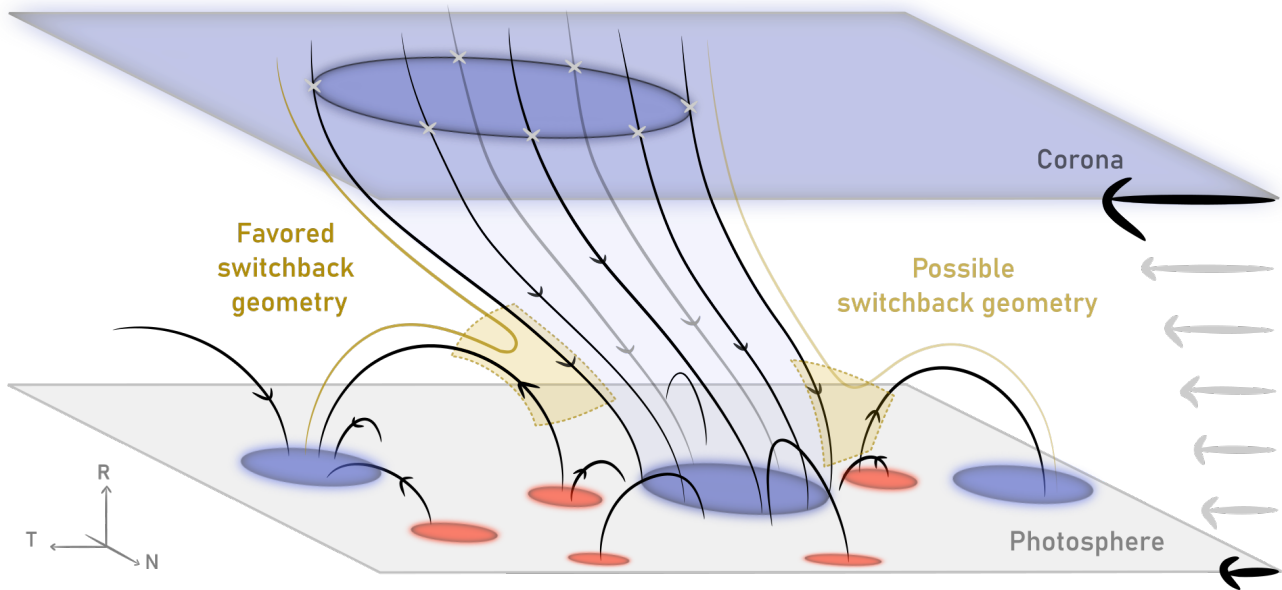


Fig. 10. Illustration of a possible explanation for the preferential orientation of a switchback, assuming interchange reconnection in the low corona as the initial mechanism. The sketch displays an element of open flux tubes from the photosphere expanding out into a faster corona, along closed loops that form the magnetic carpet. The blue (red) color is associated with the negative (positive) polarity of the field lines. Some potential reconnection sites are highlighted in light yellow (non-exhaustive) and reconnected field lines are displayed in yellow. The arrows on the right highlight the relative speed gradient that exists between the differentially rotating photosphere and the quasi-rigidly rotating corona.

Regarding the bias in elevation, [Fisk et al. \(1999\)](#) interestingly highlight a potential circulation of field line footpoints at the photosphere from the poles toward the equator, which would be consistent with the slight bias we find toward negative θ values (i.e., negative B_N ; see Fig. 9b). Indeed, a field line rooted in the northern (southern) hemisphere would then be dragged downward (upward) and favor reconnection in the configurations displayed in Fig. 9b. However, considering that the bias we find in $-\theta$ is small, we advise caution in the interpretation of this result and consider it less robust than the bias found in the ecliptic plane.

The preferential orientation we find – for switchbacks to deflect in the clockwise direction – does not seem to fit with a formation process involving either solely solar wind turbulence, as developed by [Squire et al. \(2020\)](#), [Mallet et al. \(2021\)](#), and [Shoda et al. \(2021\)](#), or in situ velocity shears, as developed by [Ruffolo et al. \(2020\)](#). It seems that both of these processes would produce fluctuations that should appear as rather isotropic in the data. However, most of the studies cited above focus on the radial component of the magnetic field only. An analysis of the distribution of the magnetic field orientation angles in simulations from [Squire et al. \(2020\)](#), [Mallet et al. \(2021\)](#), and [Shoda et al. \(2021\)](#) (for turbulent generation) and [Ruffolo et al. \(2020\)](#) (for in situ velocity shears) would be of interest here, to investigate whether these other mechanisms can also introduce anisotropy in switchback properties.

We conclude that our results seem overall consistent with interchange reconnection in the low atmosphere being a plausible source of the preferential orientation of switchbacks. The bias we find helps reconcile the differential rotation of the photosphere and a more rigid rotation of the corona. We point out that we studied the switchback phenomenon in a probabilistic approach, without identifying exact structures in the data. Hence, we cannot conclude if the bias we find is due to switchbacks appearing more frequently in this direction, or if longer switchbacks tend to orient themselves in this direction. Finally,

we realize that our study is not sufficient to determine how reconnection would create, propagate, and preserve the switchbacks all the way to PSP’s location (see [Tenerani et al. 2020](#) for instance). Several explanations stemming from interchange reconnection are currently being investigated. We here provide an additional observational constraint, consistent with the results from [Horbury et al. \(2020\)](#), that models and simulations should reproduce.

7. Conclusion

We investigate a potential preferred orientation in the large magnetic deflections called switchbacks.

We first caution that, by construction, the choice of definition used to identify a magnetic switchback impacts the results (Sect. 2.2). We chose to consider fluctuations away from the Parker spiral by using a locally defined Parker frame and two orientation angles in azimuth (ϕ) and elevation (θ) (Sect. 2.3).

We characterize the quiet solar wind orientation (Sect. 3) and find that the Parker spiral model indeed remains accurate at such short distances from the Sun. We notice that an offset appears for the latest encounters (E_8 and E_9) and is linked to the lower radial distance. This is expected and shows that PSP is located near the acceleration region of the solar wind.

We then investigated the large fluctuation orientation (Sect. 4.1). To do so, we assumed that the wind was composed of two populations with distinct distribution properties, respectively representing the background and perturbed solar winds. We assumed a normal distribution of orientation angles for both distributions and fit our data with this model. This method allows us to define the switchback population without having to choose an arbitrary threshold in the magnetic field deviation. We find that the actual distribution of orientation angles is well reproduced using this method. We derived from this fit that the mean value of the switchback population is biased by a few degrees toward lower ϕ for all encounters except E_6 (a -5.5° shift on

average), and toward lower θ for all encounters except E_2 and E_6 (a -2.1° shift on average; see Fig. 7 and Table 3). This occurs regardless of the main polarity of the field. We conclude that switchbacks occur in all directions but present a preferential orientation in the $-\phi$ direction (clockwise)*, and to a lesser extent in the $-\theta$ direction (toward the equator).

We report the observation of a patch of magnetic switchbacks that consistently deflected in the same direction over 16 h. The deflections are all contained within the ecliptic plane and are one-sided with respect to the Parker spiral.

We discuss the implications of the preferred orientation we find (Sect. 6), showing that it favors an invariant geometry in the equatorial plane associated with a clockwise rotation and positive V_t flows, while it may favor a symmetrical geometry north and south of the HCS (Fig. 9). These results are globally consistent with the observations of Horbury et al. (2020), Macneil et al. (2020), and Meng et al. (2022). The bias in $-\phi$ might find its cause in the interchange reconnection process occurring in the low corona, which would reconcile the shear induced by the different rotation rates of the photosphere and the corona.

Acknowledgements. We acknowledge the NASA Parker Solar Probe Mission and particularly the FIELDS team led by S. D. Bale and the SWEAP team led by J. Kasper for use of data. Parker Solar Probe was designed, built, and is now operated by the Johns Hopkins Applied Physics Laboratory as part of NASA's Living with a Star (LWS) program (contract NNN06AA01C). Support from the LWS management and technical team has played a critical role in the success of the Parker Solar Probe mission. The data used in this study are available at the NASA Space Physics Data Facility (SPDF): <https://spdf.gsfc.nasa.gov>, and at the PSP science gateway <https://spggway.jhuapl.edu/>. We visualize data using the CLWeb software (<http://clweb.irap.omp.eu/>) developed by E. Penou; as well as the AMDA science analysis system (<http://amda.cdpp.eu/>) provided by the Centre de Données de la Physique des Plasmas (CDPP) supported by CNRS, CNES, Observatoire de Paris and Université Paul Sabatier (UPS), Toulouse. Work at IRAP was supported by CNRS, CNES and UPS. The work of A. P. Rouillard and V. Réville was funded by the ERC SLOW_SOURCE project (SLOW_SOURCE?DLV-819189). The author N. Fargette acknowledges the support of the ISSI team, working in unraveling solar wind microphysics in the inner heliosphere. The author N. Fargette would finally like to acknowledge and thank P. Houdayer for helpful hindsight and discussions, as well as participation in the technical design of Fig. 10.

References

- Akhavan-Tafti, M., Kasper, J., Huang, J., & Bale, S. 2021, *A&A*, 650, A4
- Badman, S. T., Bale, S. D., Martínez Oliveros, J. C., et al. 2020, *ApJS*, 246, 23
- Badman, S. T., Bale, S. D., Rouillard, A. P., et al. 2021, *A&A*, 650, A18
- Bagashvili, S. R., Shergelashvili, B. M., Japaridze, D. R., et al. 2017, *A&A*, 603, A134
- Bale, S. D., Goetz, K., Harvey, P. R., et al. 2016, *Space Sci. Rev.*, 204, 49
- Bale, S. D., Badman, S. T., Bonnell, J. W., et al. 2019, *Nature*, 576, 237
- Bale, S. D., Horbury, T. S., Velli, M., et al. 2021, *ApJ*, 923, 174
- Balogh, A., Forsyth, R. J., Lucek, E. A., Horbury, T. S., & Smith, E. J. 1999, *Geophys. Rev. Lett.*, 26, 631
- Bandyopadhyay, R., Matthaeus, W. H., McComas, D. J., et al. 2021, *A&A*, 650, L4
- Bourouaine, S., Perez, J. C., Klein, K. G., et al. 2020, *ApJ*, 904, L30
- Bruno, R., & Bavassano, B. 1997, *Geophys. Rev. Lett.*, 24, 2267
- Case, A. W., Kasper, J. C., Stevens, M. L., et al. 2020, *ApJS*, 246, 43
- Drake, J. F., Agapitov, O., Swisdak, M., et al. 2021, *A&A*, 650, A2
- Dudok de Wit, T., Krasnoselskikh, V. V., Bale, S. D., et al. 2020, *ApJS*, 246, 39
- Fargette, N., Lavraud, B., Rouillard, A. P., et al. 2021, *ApJ*, 919, 96
- Fisk, L. A. 1996, *J. Geophys. Res.*, 101, 15547
- Fisk, L. A., & Kasper, J. C. 2020, *ApJ*, 894, L4
- Fisk, L. A., Zurbuchen, T. H., & Schwadron, N. A. 1999, *ApJ*, 521, 868
- Foreman-Mackey, D., Farr, W., Sinha, M., et al. 2019, *J. Open Source Softw.*, 4, 1864
- Giordano, S., & Mancuso, S. 2008, *ApJ*, 688, 656
- Gosling, J. T., Tian, H., & Phan, T. D. 2011, *ApJ*, 737, L35
- Horbury, T. S., Matteini, L., & Stansby, D. 2018, *MNRAS*, 478, 1980
- Horbury, T. S., Woolley, T., Laker, R., et al. 2020, *ApJS*, 246, 45
- Kasper, J. C., Abiad, R., Austin, G., et al. 2016, *Space Sci. Rev.*, 204, 131
- Kasper, J. C., Bale, S. D., Belcher, J. W., et al. 2019, *Nature*, 576, 228
- Kasper, J. C., Klein, K. G., Lichko, E., et al. 2021, *Phys. Lett. Rev.*, 127, 255101
- Laker, R., Horbury, T. S., Bale, S. D., et al. 2021, *A&A*, 650, A1
- Larosa, A., Krasnoselskikh, V., Dudok de Wit, T., et al. 2021, *A&A*, 650, A3
- Lionello, R., Riley, P., Linker, J. A., & Mikić, Z. 2005, *ApJ*, 625, 463
- Lionello, R., Linker, J. A., Mikić, Z., & Riley, P. 2006, *ApJ*, 642, L69
- Livi, R., Larson, D. E., Kasper, J. C., et al. 2021, *Earth Space Sci. Open Archive*, 20
- Macneil, A. R., Owens, M. J., Wicks, R. T., et al. 2020, *MNRAS*, 494, 3642
- Mallet, A., Squire, J., Chandran, B. D. G., Bowen, T., & Bale, S. D. 2021, *ApJ*, 918, 62
- Mancuso, S., & Giordano, S. 2011, *ApJ*, 729, 79
- Mancuso, S., Giordano, S., Barghini, D., & Telloni, D. 2020, *A&A*, 644, A18
- Martinović, M. M., Klein, K. G., Huang, J., et al. 2021, *ApJ*, 912, 28
- Matteini, L., Horbury, T. S., Neugebauer, M., & Goldstein, B. E. 2014, *Geophys. Rev. Lett.*, 41, 259
- Meng, M.-M., Liu, Y. D., Chen, C., & Wang, R. 2022, *Res. Astrophys. Astron.*, 22, 035018
- Mozer, F. S., Agapitov, O. V., Bale, S. D., et al. 2020, *ApJS*, 246, 68
- Nash, A. G., Sheeley, N. R. Jr., & Wang, Y. M. 1988, *Sol. Phys.*, 117, 359
- Owens, M. J., Lockwood, M., Barnard, L. A., & MacNeil, A. R. 2018, *ApJ*, 868, L14
- Owens, M., Lockwood, M., Macneil, A., & Stansby, D. 2020, *Sol. Phys.*, 295, 37
- Parker, E. N. 1958, *ApJ*, 128, 664
- Phan, T. D., Bale, S. D., Eastwood, J. P., et al. 2020, *ApJS*, 246, 34
- Réville, V., Velli, M., Panasenco, O., et al. 2020, *ApJS*, 246, 24
- Ruffolo, D., Matthaeus, W. H., Chhiber, R., et al. 2020, *ApJ*, 902, 94
- Schwadron, N. A., & McComas, D. J. 2021, *ApJ*, 909, 95
- Shoda, M., Chandran, B. D. G., & Cranmer, S. R. 2021, *ApJ*, 915, 52
- Squire, J., Chandran, B. D. G., & Meyrand, R. 2020, *ApJ*, 891, L2
- Sterling, A. C., & Moore, R. L. 2020, *ApJ*, 896, L18
- Tenerani, A., Velli, M., Matteini, L., et al. 2020, *ApJS*, 246, 32
- Wang, Y. M., & Sheeley, N. R. Jr. 2004, *ApJ*, 612, 1196
- Wang, Y. M., Nash, A. G., & Sheeley, N. R. Jr. 1989, *Science*, 245, 712
- Wang, Y. M., Hawley, S. H., & Sheeley, N. R. Jr. 1996, *Science*, 271, 464
- Whittlesey, P. L., Larson, D. E., Kasper, J. C., et al. 2020, *ApJS*, 246, 74
- Woodham, L. D., Horbury, T. S., Matteini, L., et al. 2021, *A&A*, 650, L1
- Woolley, T., Matteini, L., Horbury, T. S., et al. 2020, *MNRAS*, 498, 5524
- Wu, H., Tu, C., Wang, X., & Yang, L. 2021, *ApJ*, 911, 73
- Zank, G. P., Nakanotani, M., Zhao, L. L., Adhikari, L., & Kasper, J. 2020, *ApJ*, 903, 1

Appendix A: Quiet wind intervals

Table A.1. continued.

Table A.1. Timetable of quiet solar wind intervals manually selected over encounters 1, 2, 4, 5, 6, 7, 8, and 9 (see Sect. 3)

Enc	Start time	End time
1	2018-10-31T23:17:00	2018-11-01T01:28:00
1	2018-11-01T14:00:00	2018-11-01T17:00:00
1	2018-11-02T08:00:00	2018-11-02T12:00:00
1	2018-11-02T13:18:00	2018-11-02T17:00:00
1	2018-11-02T20:37:00	2018-11-02T23:25:00
1	2018-11-03T02:40:00	2018-11-03T05:15:00
1	2018-11-03T14:58:00	2018-11-03T20:52:00
1	2018-11-04T17:40:00	2018-11-05T01:23:00
1	2018-11-05T18:00:00	2018-11-05T23:00:00
1	2018-11-07T03:59:00	2018-11-07T05:56:00
1	2018-11-08T07:04:00	2018-11-08T09:10:00
1	2018-11-08T10:04:00	2018-11-08T12:07:00
1	2018-11-08T17:46:00	2018-11-08T20:47:00
1	2018-11-10T10:25:00	2018-11-10T18:31:00
1	2018-11-11T00:00:00	2018-11-11T17:00:00
2	2019-03-30T18:00:00	2019-03-30T19:18:00
2	2019-03-30T21:10:00	2019-03-30T22:00:00
2	2019-04-01T06:00:00	2019-04-01T09:00:00
2	2019-04-01T18:16:00	2019-04-01T21:47:00
2	2019-04-02T06:46:00	2019-04-02T08:14:00
2	2019-04-02T10:34:00	2019-04-02T11:43:00
2	2019-04-02T14:04:00	2019-04-02T15:06:00
2	2019-04-02T18:07:47	2019-04-02T18:59:53
2	2019-04-03T02:31:00	2019-04-03T03:23:00
2	2019-04-03T08:00:00	2019-04-03T11:00:00
2	2019-04-03T13:00:00	2019-04-03T20:00:00
2	2019-04-03T23:02:00	2019-04-04T01:43:00
2	2019-04-04T04:43:00	2019-04-04T06:50:00
2	2019-04-04T15:06:00	2019-04-04T16:22:00
2	2019-04-04T17:59:00	2019-04-04T18:55:00
2	2019-04-05T18:46:00	2019-04-06T00:32:00
2	2019-04-06T10:00:00	2019-04-06T13:00:00
2	2019-04-07T10:00:00	2019-04-07T19:00:00
2	2019-04-08T18:09:00	2019-04-08T20:18:00
2	2019-04-09T19:00:00	2019-04-09T20:29:00
2	2019-04-10T14:59:00	2019-04-10T17:31:00
2	2019-04-11T09:00:00	2019-04-11T12:00:00
4	2020-01-22T15:00:00	2020-01-22T16:00:00
4	2020-01-23T15:00:00	2020-01-23T16:00:00
4	2020-01-23T17:05:00	2020-01-23T18:38:00
4	2020-01-23T23:04:00	2020-01-24T00:53:00
4	2020-01-24T05:00:00	2020-01-24T06:00:00
4	2020-01-24T16:00:00	2020-01-24T19:00:00
4	2020-01-25T06:01:21	2020-01-25T06:55:26
4	2020-01-25T23:00:00	2020-01-26T00:32:00
4	2020-01-26T05:04:00	2020-01-26T06:58:00
4	2020-01-26T14:00:00	2020-01-26T15:00:00
4	2020-01-27T05:19:00	2020-01-27T06:41:00
4	2020-01-28T05:00:00	2020-01-28T06:00:00
4	2020-01-28T10:00:00	2020-01-28T12:00:00
4	2020-01-28T23:59:00	2020-01-29T01:35:00
4	2020-01-29T01:44:00	2020-01-29T03:00:00
4	2020-01-29T11:00:00	2020-01-29T13:00:00
4	2020-01-29T16:00:00	2020-01-29T23:00:00
4	2020-01-30T05:39:00	2020-01-30T06:56:00

Enc	Start time	End time
4	2020-01-30T07:04:00	2020-01-30T08:50:00
4	2020-01-30T09:09:00	2020-01-30T11:00:00
4	2020-01-30T12:00:00	2020-01-30T13:00:00
4	2020-01-30T22:00:00	2020-01-31T01:00:00
4	2020-01-31T12:17:00	2020-01-31T17:59:00
4	2020-02-01T20:11:43	2020-02-01T20:59:39
4	2020-02-02T00:00:00	2020-02-02T01:42:00
4	2020-02-02T10:00:00	2020-02-02T12:00:00
4	2020-02-03T14:00:00	2020-02-03T17:00:00
5	2020-06-01T07:00:00	2020-06-01T09:00:00
5	2020-06-01T16:53:00	2020-06-01T18:10:00
5	2020-06-02T00:10:00	2020-06-02T04:54:00
5	2020-06-02T20:14:00	2020-06-03T00:04:00
5	2020-06-03T16:13:00	2020-06-03T17:51:00
5	2020-06-04T00:55:00	2020-06-04T03:17:00
5	2020-06-04T06:21:00	2020-06-04T07:32:00
5	2020-06-04T10:19:00	2020-06-04T12:12:00
5	2020-06-04T18:04:00	2020-06-04T19:43:00
5	2020-06-06T09:41:00	2020-06-06T12:25:00
5	2020-06-07T00:27:00	2020-06-07T02:01:00
5	2020-06-07T04:19:00	2020-06-07T06:14:00
5	2020-06-07T10:00:00	2020-06-07T11:00:00
5	2020-06-07T13:00:00	2020-06-07T15:00:00
5	2020-06-07T16:00:00	2020-06-07T19:00:00
5	2020-06-08T12:48:00	2020-06-08T15:24:00
5	2020-06-09T03:13:00	2020-06-09T04:52:00
5	2020-06-09T05:45:00	2020-06-09T07:36:00
5	2020-06-10T05:00:00	2020-06-10T23:00:00
5	2020-06-11T09:00:00	2020-06-12T01:00:00
5	2020-06-13T09:00:00	2020-06-13T12:00:00
5	2020-06-13T16:00:00	2020-06-14T01:00:00
6	2020-09-21T04:15:01	2020-09-21T07:06:00
6	2020-09-21T12:41:00	2020-09-21T15:33:00
6	2020-09-22T08:13:00	2020-09-22T11:54:00
6	2020-09-24T21:00:00	2020-09-25T08:00:00
6	2020-09-25T19:33:00	2020-09-25T21:13:00
6	2020-09-26T04:26:00	2020-09-26T05:09:00
6	2020-09-26T06:11:00	2020-09-26T08:15:00
6	2020-09-26T09:29:00	2020-09-26T12:30:00
6	2020-09-27T03:06:00	2020-09-27T05:15:00
6	2020-09-27T10:03:00	2020-09-27T11:04:00
6	2020-09-27T18:46:00	2020-09-27T21:46:00
6	2020-09-29T02:04:00	2020-09-29T03:49:00
6	2020-09-29T08:00:00	2020-09-29T10:00:00
6	2020-09-29T15:00:00	2020-09-29T18:00:00
6	2020-09-29T22:00:00	2020-09-30T07:00:00
6	2020-10-01T00:00:00	2020-10-01T06:00:00
6	2020-10-01T20:00:00	2020-10-02T01:00:00
6	2020-10-02T15:00:00	2020-10-02T20:00:00
6	2020-10-03T06:39:00	2020-10-03T09:47:00
7	2021-01-11T09:04:00	2021-01-11T10:29:00
7	2021-01-11T13:32:00	2021-01-11T14:31:00
7	2021-01-13T00:00:00	2021-01-13T01:00:00
7	2021-01-13T08:00:00	2021-01-13T11:00:00
7	2021-01-14T03:00:00	2021-01-14T08:00:00
7	2021-01-15T00:00:00	2021-01-15T03:00:00
7	2021-01-15T18:22:00	2021-01-15T22:22:00
7	2021-01-16T00:12:00	2021-01-16T01:44:00
7	2021-01-16T02:09:00	2021-01-16T04:15:00

Table A.1. continued.

Enc	Start time	End time
7	2021-01-16T05:09:00	2021-01-16T07:14:00
7	2021-01-16T09:44:00	2021-01-16T11:08:00
7	2021-01-16T23:02:00	2021-01-17T00:16:00
7	2021-01-17T09:00:00	2021-01-17T13:00:00
7	2021-01-17T16:03:00	2021-01-17T17:25:00
7	2021-01-18T08:47:00	2021-01-18T10:08:00
7	2021-01-19T01:23:00	2021-01-19T02:59:00
7	2021-01-19T03:45:00	2021-01-19T05:11:00
7	2021-01-19T12:39:00	2021-01-19T13:24:00
7	2021-01-19T23:39:00	2021-01-20T07:20:00
7	2021-01-21T13:00:00	2021-01-21T18:00:00
8	2021-04-24T05:00:00	2021-04-24T14:16:00
8	2021-04-26T04:24:00	2021-04-26T06:31:00
8	2021-04-26T11:00:00	2021-04-26T12:48:00
8	2021-04-26T13:22:00	2021-04-26T15:11:00
8	2021-04-26T19:28:00	2021-04-26T21:11:00
8	2021-04-27T15:00:00	2021-04-27T17:00:00
8	2021-04-28T04:23:00	2021-04-28T05:43:00
8	2021-04-28T10:00:00	2021-04-28T12:00:00
8	2021-04-28T13:05:00	2021-04-28T16:45:00
8	2021-04-28T19:00:00	2021-04-28T21:00:00
8	2021-04-29T02:01:00	2021-04-29T03:32:00
8	2021-04-29T06:30:00	2021-04-29T08:09:00
8	2021-04-29T20:35:00	2021-04-30T05:28:00
8	2021-05-01T17:41:00	2021-05-01T22:24:00
8	2021-05-03T04:19:00	2021-05-03T06:42:00
9	2021-08-04T20:00:00	2021-08-05T08:00:00
9	2021-08-05T13:31:00	2021-08-05T16:54:00
9	2021-08-06T09:31:00	2021-08-06T11:58:00
9	2021-08-07T14:16:00	2021-08-08T02:49:00
9	2021-08-08T10:53:00	2021-08-08T11:54:00
9	2021-08-08T17:20:00	2021-08-08T18:43:00
9	2021-08-08T21:07:00	2021-08-08T22:46:00
9	2021-08-09T09:16:00	2021-08-09T10:01:00
9	2021-08-09T16:52:00	2021-08-09T19:56:00
9	2021-08-09T21:03:00	2021-08-10T00:27:00
9	2021-08-10T08:42:00	2021-08-10T10:36:00
9	2021-08-10T11:37:00	2021-08-10T12:29:00
9	2021-08-10T18:54:00	2021-08-11T01:03:00
9	2021-08-11T11:00:00	2021-08-11T14:00:00
9	2021-08-11T18:00:00	2021-08-11T19:00:00
9	2021-08-11T20:36:00	2021-08-11T22:21:00
9	2021-08-11T23:59:00	2021-08-12T01:19:00
9	2021-08-12T05:39:00	2021-08-12T06:45:00
9	2021-08-12T19:05:00	2021-08-12T20:02:00
9	2021-08-14T03:00:00	2021-08-14T06:00:00
9	2021-08-14T22:59:00	2021-08-15T00:15:00
9	2021-08-15T01:58:00	2021-08-15T03:34:00

Appendix B: Discarded intervals

We give in the following table the list of intervals that were discarded in our study during the different encounters. They correspond to HCS crossings, heliospheric plasma sheet (HPS) crossings, CMEs, FRs, or periods of strahl drop-out (i.e., periods when the strahl disappears), where magnetic field lines are most likely disconnected from the Sun. All of these intervals were identified visually while scanning through the data. Inter-

Table B.1. Timetable of discarded intervals manually selected over encounters 1, 2, 4, 5, 6, 7, 8, and 9.

Enc	Start time	End time	Tag
1	2018-10-31T04:00	10-31T12:20	CME
1	2018-11-11T17:00	11-12T12:00	CME
4	2020-01-30T13:15	01-30T17:10	HPS
4	2020-01-31T19:50	02-01T00:05	HPS
4	2020-02-01T03:55	02-01T04:15	HCS
5	2020-05-31T12:21	06-01T03:40	Flux ropes
5	2020-06-01T10:00	06-01T16:10	Strahl inversion
5	2020-06-01T19:35	06-01T21:35	Flux rope
5	2020-06-02T06:50	06-02T09:10	HPS
5	2020-06-04T03:25	06-04T06:05	HPS
5	2020-06-07T11:10	06-07T12:40	HPS
5	2020-06-07T20:20	06-07T21:10	HPS
5	2020-06-08T00:40	06-08T12:30	HCS
5	2020-06-08T15:30	06-09T01:40	HCS
5	2020-06-12T01:00	06-12T08:00	Flux rope or CME
6	2020-09-20T11:00	09-22T08:00	multiple HCS
6	2020-09-25T08:40	09-25T19:22	HCS
6	2020-09-25T08:40	09-25T19:22	HCS
6	2020-09-30T09:00	09-30T18:00	probable HCS
7	2021-01-17T13:00	01-17T15:00	HCS
7	2021-01-19T13:24	01-19T23:50	HCS
7	2021-01-20T07:20	01-20T14:00	compressible structure
7	2021-01-22T21:00	01-24T12:30	HCS
8	2021-04-23T22:20	04-24T04:00	HCS
8	2021-04-24T15:57	04-24T16:18	HCS
8	2021-04-29T00:30	04-29T02:01	HCS
8	2021-04-29T07:40	04-29T10:59	HCS
8	2021-04-29T13:38	04-29T14:00	HCS
9	2021-08-10T00:27	08-10T01:54	HCS
9	2021-08-10T10:34	08-10T12:06	HCS
9	2021-08-10T13:50	08-10T18:54	HCS

vals from E_1 to E_5 were previously identified in [Fargette et al. \(2021\)](#).

Appendix C: Fitting results

In Sect. 4 we sample the parameter space using the *emcee*² python library ([Foreman-Mackey et al. 2019](#)), which is based on a Monte Carlo Markov chain algorithm. We used 32 walkers and 2000 iterations and used the *Chain Consumer*³ library to visualize the fitting results. In Fig. C.1 we display the convergence of the fitting algorithm over 2000 iterations. After 1000 steps the results are stable, and so we display the probability distribution function of walker positions in Fig. C.2, discarding the first 1000 iterations.⁴ The fitting results for all encounters are available in Table C.1

² <https://emcee.readthedocs.io/en/stable/>

³ https://samreay.github.io/ChainConsumer/chain_api.html

⁴ The associated python code is available here: [fit_double_gaussian.py](#)

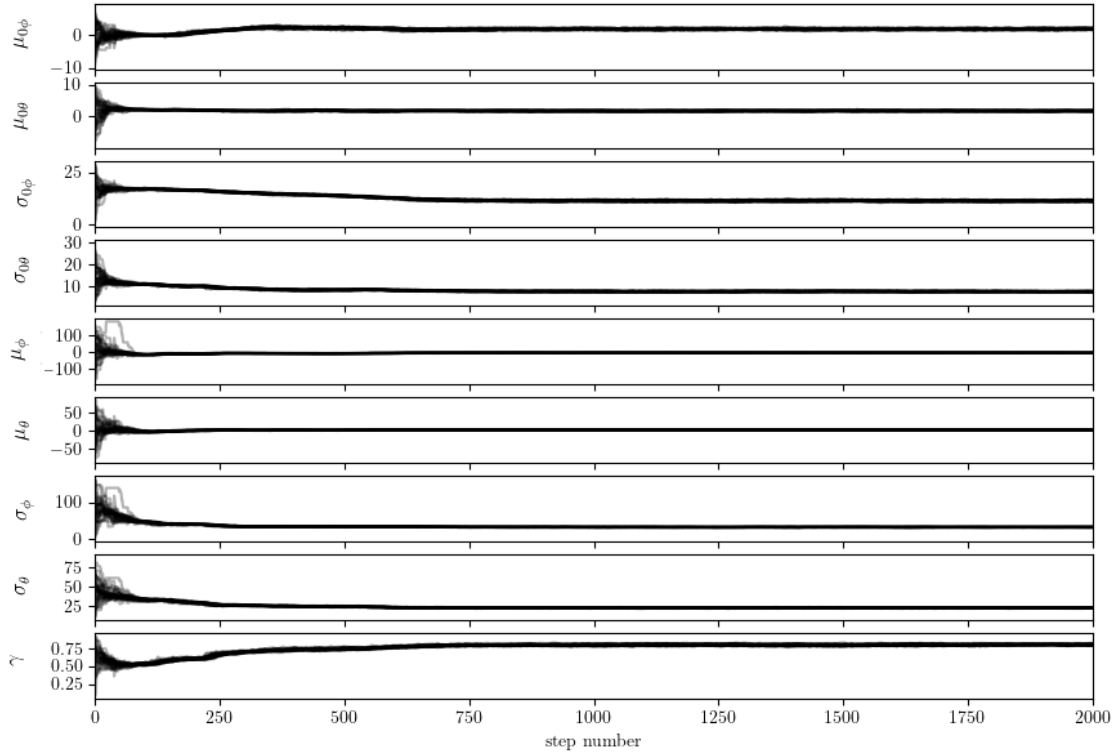
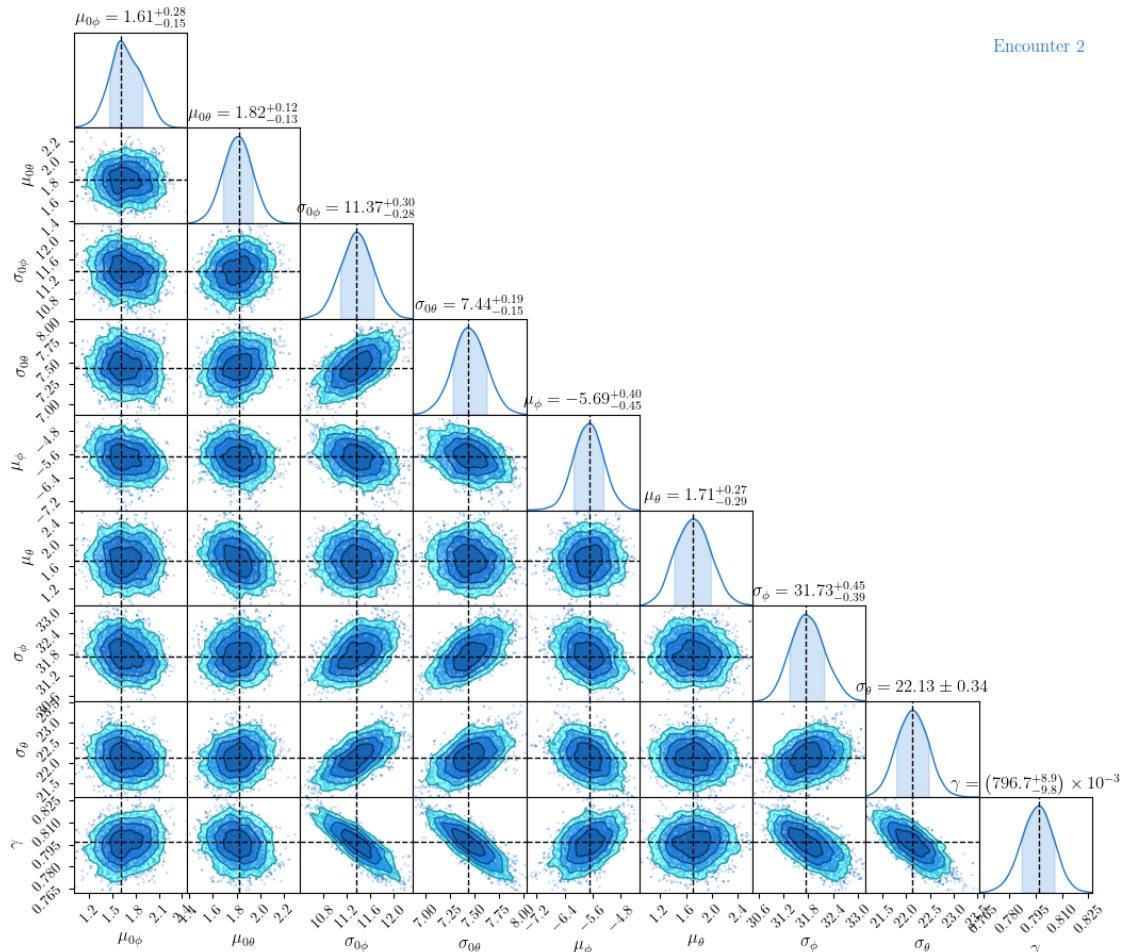


Fig. C.1. Walker path in the parameter space over 2000 iterations.



Encounter 2

Fig. C.2. 9D probability distribution function of walker positions, discarding the first 1000 iterations.

Table C.1. Most probable (maximum a posteriori) parameter vectors, \mathbf{P} , obtained after fitting the double Gaussian model described in the text to the data for all the encounters.

Enc	$\mu_{0\phi}$	$\mu_{0\theta}$	$\sigma_{0\phi}$	$\sigma_{0\theta}$	μ_{ϕ}	μ_{θ}	σ_{ϕ}	σ_{θ}	γ
1	$0.04^{+0.16}_{-0.20}$	$1.17^{+0.14}_{-0.16}$	$12.39^{+0.30}_{-0.38}$	10.53 ± 0.24	$-5.37^{+0.54}_{-0.38}$	$-0.06^{+0.28}_{-0.34}$	$34.77^{+0.66}_{-0.59}$	$25.01^{+0.41}_{-0.38}$	$0.755^{+0.01}_{-0.002}$
2	$1.61^{+0.28}_{-0.15}$	$1.82^{+0.12}_{-0.13}$	$11.37^{+0.30}_{-0.28}$	$7.44^{+0.19}_{-0.15}$	$-5.69^{+0.40}_{-0.45}$	$1.71^{+0.27}_{-0.29}$	$31.73^{+0.45}_{-0.39}$	22.13 ± 0.34	$0.797^{+0.009}_{-0.01}$
4	$0.69^{+0.16}_{-0.14}$	$1.711^{+0.109}_{-0.099}$	$14.04^{+0.26}_{-0.17}$	$10.75^{+0.14}_{-0.15}$	-0.89 ± 0.50	$0.24^{+0.39}_{-0.44}$	$34.51^{+0.70}_{-0.69}$	$24.62^{+0.50}_{-0.46}$	$0.598^{+0.012}_{-0.017}$
5	$3.85^{+0.18}_{-0.17}$	$2.60^{+0.11}_{-0.12}$	$14.23^{+0.20}_{-0.18}$	$10.19^{+0.16}_{-0.15}$	$-7.59^{+0.86}_{-0.63}$	$-1.33^{+0.44}_{-0.63}$	$33.37^{+0.64}_{-0.66}$	$26.42^{+0.50}_{-0.45}$	0.603 ± 0.012
6	$2.11^{+0.15}_{-0.14}$	$1.642^{+0.096}_{-0.090}$	$12.46^{+0.22}_{-0.23}$	$7.99^{+0.15}_{-0.13}$	$1.79^{+0.37}_{-0.38}$	$1.46^{+0.25}_{-0.22}$	$27.80^{+0.47}_{-0.51}$	$18.50^{+0.41}_{-0.30}$	0.660 ± 0.016
7	$0.51^{+0.14}_{-0.19}$	$2.778^{+0.098}_{-0.068}$	$14.22^{+0.16}_{-0.21}$	$7.56^{+0.14}_{-0.12}$	-7.46 ± 0.49	$-2.81^{+0.38}_{-0.40}$	$33.83^{+0.56}_{-0.48}$	$24.71^{+0.40}_{-0.32}$	$0.688^{+0.0074}_{-0.0094}$
8	$-5.15^{+0.15}_{-0.13}$	$1.161^{+0.093}_{-0.078}$	$10.91^{+0.16}_{-0.17}$	$6.886^{+0.097}_{-0.124}$	$-11.98^{+0.49}_{-0.56}$	$-1.76^{+0.30}_{-0.43}$	$37.35^{+0.57}_{-0.50}$	$26.71^{+0.46}_{-0.34}$	$0.760^{+0.0055}_{-0.0057}$
9	$-6.57^{+0.16}_{-0.18}$	$-0.73^{+0.11}_{-0.10}$	$9.93^{+0.26}_{-0.24}$	$7.31^{+0.16}_{-0.18}$	$-9.67^{+0.40}_{-0.45}$	$-2.75^{+0.32}_{-0.37}$	$25.29^{+0.58}_{-0.47}$	$19.66^{+0.41}_{-0.45}$	0.707 ± 0.015